ACS OMEGA

http://pubs.acs.org/journal/acsodf

Article

High Intrinsic Phosphorescence Efficiency and Density Functional Theory Modeling of Ru(II)-Bipyridine Complexes with π-Aromatic-Rich Cyclometalated Ligands: Attributions of Spin−Orbit Coupling Perturbation and Efficient Configurational Mixing of Singlet Excited States

Yu Ru Chih,[†] Yu-Ting Lin,[†] Chi-Wei Yin,[†] and Yuan Jang Chen*

Cite This: *ACS Omega* 2022, 7, 48583−48599

Read Online

ACCESS | Metrics & More | Article Recommendations | Supporting Information

ABSTRACT: A series of π-aromatic-rich cyclometalated ruthenium(II)-(2,2′-bipyridine) complexes ($[Ru(bpy)_2(\pi_{Ar}\text{-CM})]^+$) in which π_{Ar}-CM is diphenylpyrazine or 1-phenylisoquinoline were prepared. The $[Ru(bpy)_2(\pi_{Ar}\text{-CM})]^+$ complexes had remarkably high phosphorescence rate constants, $k_{RAD(p)}$, and the intrinsic phosphorescence efficiencies ($\iota_{em(p)} = k_{RAD(p)}/(\nu_{em(p)})^3$) of these complexes were found to be twice the magnitudes of simply constructed cyclometalated ruthenium(II) complexes ($[Ru(bpy)_2(sc\text{-CM})]^+$), where $\nu_{em(p)}$ is the phosphorescence frequency and sc-CM is 2-phenylpyridine, benzo[*h*]quinoline, or 2-phenylpyrimidine. Density functional theory (DFT) modeling of the $[Ru(bpy)_2(CM)]^+$ complexes indicated numerous singlet metal-to-ligand charge transfers for ^{1}MLCT-(Ru-bpy) and ^{1}MLCT-(Ru-CM), excited states in the low-energy absorption band and $^1\pi\pi^*$-(aromatic ligand) ($^1\pi\pi^*$-L_{Ar}) excited states in the high-energy band. DFT modeling of these complexes also indicated phosphorescence-emitting state (T_e) configurations with primary MLCT-(Ru-bpy) characteristics. The variation in $\iota_{em(p)}$ for the spin-forbidden T_e (^{3}MLCT-(Ru-bpy)) excited state of the complex system that was examined in this study can be understood through the spin−orbit coupling (SOC)-mediated sum of intensity stealing (∑SOCM-IS) contribution from the primary intensity of the low-energy ^{1}MLCT states and second-order intensity perturbation from the significant configuration between the low-energy ^{1}MLCT and high-energy intense $^1\pi\pi^*$-L_{Ar} states. In addition, the observation of unusually high $\iota_{em(p)}$ magnitudes for these $[Ru(bpy)_2(\pi_{Ar}\text{-CM})]^+$ complexes can be attributed to the values for both intensity factors in the ∑SOCM-IS formalism being individually greater than those for $[Ru(bpy)_2(sc\text{-CM})]^+$ ions.

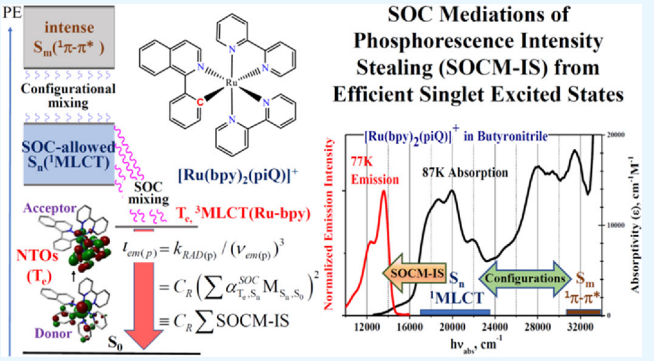

INTRODUCTION

Since the pioneering work on the photophysical mechanics of the excited states of transition metal-diimine complexes by Demas and Crosby nearly half a century ago,[1−3] fundamental investigations related to the excited-state relaxation of low-spin transition metal aromatic-ligand-acceptor chromophores (M-L_{Ar}) has been of interest in studies on photophysical relaxation of excited states,[2−5] low-energy triplet metal center (^{3}MC) relaxation,[6−9] spin−orbit coupling (SOC)[10−12]-mediated configurational mixing between emitting triplet and efficient singlet excited states (SOCM),[13−16] and photocatalysis,[17−19] where M in M-L_{Ar} is a transition metal element (ion) with a relatively high atomic number. It should be noted in this respect that the photoinduced relaxation of M-L_{Ar}-type chromophores has found applications in solar energy conversion,[20−24] organic light-emitting diodes (OLEDs),[25−31] and photodynamic therapy for the treatment of cancer.[32−42] The photoinduced excited-state relaxation of molecules in an action model includes[12−14,43−56] (1) internal conversion (k_{ic}) between states with the same spin multiplicity and intersystem crossing (k_{isc}) between states with different spin multiplicities; (2) nonradiative relaxation (k_{NRD}) of the emitting state directly to the ground state by vibronic coupling; (3) radiative relaxation (k_{RAD}), including fluorescence (fl) and phosphorescence (p); and (4) other quenching processes (k_q), such as MC excited-state quenching.

The k_{RAD} formalism for spontaneous luminescence in a molecular system based on Einstein's expression for atomic

Received: November 12, 2022
Accepted: November 23, 2022
Published: December 14, 2022

fluorescence has appeared in numerous monographs.[12,43,44] The k_{RAD} of a chromophore model is a function of the average sum of the spectral contributions determined by the observed photonic fluorescence integration in an organic system with two states, namely, the ground state (g) and the excited state (e), and can be expressed by[12,13,44−46,50,57]

$$k_{RAD} = C_R(\nu_{em})^3(M_{e,g})^2 \quad (1)$$

where the terms in eq 1 are the transition dipole moment ($M_{e,g}$), the fluorescence frequency (ν_{em}, corresponding to the emission energy $h\nu_{em}$), and $C_R = (16\pi^3\eta^3)/(3\varepsilon_o c^3 h)$, where η is the refractive index, ε_o is the vacuum permittivity, c is the speed of light, and h is Planck's constant. The experimental k_{RAD} amplitude is obtained from the emission quantum yield, ϕ_{em}, and the observed mean of the emission lifetime, τ_{obs}, where $k_{RAD} = \phi_{em} \times k_{obs}$ and $k_{obs} = 1/\tau_{obs} = k_{RAD} + k_{NRD}$.

Phosphorescence in an ideal model is fundamentally a spin-forbidden transition, and a theoretical description of this natural phenomenon in a molecular system requires a significant $M_{e,g}$ contribution from an SOC configuration of the singlet (S_n, $n \geq 1$ in a multistate model) and triplet emitting (T_e) states, where $M_{e,g} = \alpha^{SOC}_{T_e,S_n} M_{S_n,S_0}$ and $M_{e,g} = 0$ in eq 1 for an ideal phosphorescence ($T_e \rightarrow S_0$) transition without SOC perturbation, $\alpha^{SOC}_{T_e,S_n}$ is the SOC mixing coefficient between the T_e and S_n states, and M_{S_n,S_0} is the transition dipole moment of the S_n excited state.[12,14,44,50,57,58] The configurational mixing coefficient (α) of the target electronic states in a weak mixing limit, $1 \gg \alpha^2 > 0$, can be approximated by the term $\alpha \approx H/\Delta E$,[59−64] where H and ΔE are the coupling element and the vertical energy difference between the states, respectively.

The phosphorescence of an M-L_{Ar}-type chromophore fundamentally occurs through SOC configurations,[2,14,15,65,66] so the spin−orbit coupling element (H^{SOC} in α^{SOC}) of the $T_e \rightarrow S_0$ transition is not zero. In early studies,[50,67,68] the H^{SOC} value was plausibly postulated to increase approximately with the fourth power of the atomic number (Z^4), which is a so-called heavy atom effect.[12,43] In the present SOC modeling, the differences in the spin angular momenta ($\vec{S}$) between the T_e and S_n states and the distance (r) between the nucleus (with effective nuclear charge, Z^{eff}) and the target electrons must be accompanied by a simultaneous change in the orientation of the orbital angular momenta ($\vec{L}$) for a spin−orbit operator, $\hat{H}^{SO} \propto \sum\left[\left(\frac{Z^{eff}}{r^3}\right)\vec{S}\cdot\vec{L}\right]$, in the efficient SOC configuration.[69−71] A useful SOC selection rule for phosphorescence from M-L_{Ar}-type chromophores was required in this study because the dominant SOC perturbation of the transition moment stealing ($\alpha^{SOC}_{T_e,S_{n(T)}} M_{S_{n(T)},S_0}$) is from efficient $S_{n(T)}$ states (S_n in the T_e geometry). In this case, the donor singly occupied molecular orbital (SOMO) contains a different M-dπ orbital from the donor-dπ SOMO of the triplet emitting metal-to-ligand charge-transfer state, ^{3}MLCT (T_e).[14,15,72,73] The SOC-mediated emission intensity stealing due to significant T_e/S_n mixing with a small vertical energy difference, $\Delta E_{T_e,S_n} = E(S_n)_\nu - E(T_e)_{min}$, has been widely studied in the early literature.[14,74−76]

Thus, the effective transition moment contribution for $\iota_{em(p)}$ in a molecular system is the sum of the SOC-mediated efficient singlet transitions, $|\sum \alpha^{SOC}_{T_e,S_{n(T)}} M_{S_{n(T)},S_0}|^2$, and the weak mixing coefficient ($\alpha^{SOC}_{T_e,S_{n(T)}}$) is given by[14,15,67]

$$\alpha^{SOC}_{T_e,S_{n(T)}} = \frac{\langle S_n|\hat{H}^{SO}|T_e\rangle}{E(S_n)_\nu - E(T_e)_{min}} \approx \frac{H^{SOC}_{T_e,S_{n(T)}}}{\Delta E_{T_e,S_{n(T)}}} \quad (2)$$

As a result in eq 3, the description of the intrinsic phosphorescence efficiency ($\iota_{em(p)}$) of an M-L_{Ar}-type chromophore is obtained by combining eqs 1 and 2 with $|\sum \alpha^{SOC}_{T_e,S_{n(T)}} M_{S_{n(T)},S_0}|^2$.[14,15,73]

$$\iota_{em(p)} = \frac{k_{RAD(p)}}{(\nu_{em(p)})^3} = C_R\left|\sum_{S_n}(\alpha^{SOC}_{T_e,S_{n(T)}} M_{S_{n(T)},S_0})\right|^2 \approx C_R \left|\sum_{S_n}\left(\frac{H^{SOC}_{T_e,S_{n(T)}}}{\Delta E_{T_e,S_{n(T)}}}\right)(M_{S_{n(T)},S_0})\right|^2 \quad (3)$$

The meaning of $\iota_{em(p)}$ in eq 3 can be expressed as the sum of the SOC-mediated phosphorescence intensity stealing (ΣSOCM-IS) from the efficient singlet excited states, where $\nu_{em(p)}$ corresponds to the phosphorescence energy.

A simple plot can be used to illustrate the $\iota_{em(p)}$ of the phosphorescence transitions of M-L_{Ar}-type complexes that involve an ^{3}MLCT emitting state (T_e), a singlet ground state (S_0), and efficient SOCM-IS from low-energy ($\Delta E_{T_e,S_n}$) singlet excited states ($S_{n(T)}$), as shown in Figure 1.

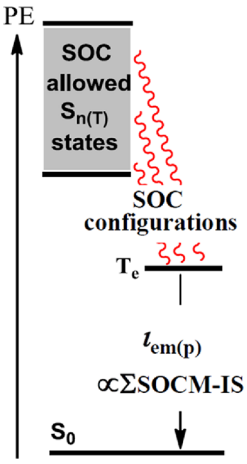

Figure 1. Jablonski-type diagram showing the phosphorescence efficiency ($\iota_{em(p)} = k_{RAD(p)}/(\nu_{em(p)})^3$) through ΣSOCM-IS contributions from efficient SOC-allowed $S_{n(T)}$ states with T_e coordinates.

Cyclometalated transition metal−polypyridine complexes have been the focus of interesting studies on photophysics and excited-state relaxation,[14,77−85] and these types of complexes have recently been applied in areas of solar energy conversion,[86−88] OLEDs,[14,89−91] and photodynamic therapy.[92,93] In previous work, the 77 K phosphorescence parameters of Ru-bpy chromophores for the cyclometalated ruthenium(II)-(2,2′-bipyridine) complexes ([Ru-(bpy)$_2$(CM)]$^+$) with a simply constructed cyclometalated (sc-CM) coordination ligand (sc-CM = 2-phenylpyridine (ppy) and benzo[h]quinoline (bhq)) showed unusually higher $\iota_{em(p)}$ values compared to those of typical [Ru-(bpy)$_{3-n}$(Am)$_{2n}$]$^{2+}$ complexes. In addition, in the case of the

https://doi.org/10.1021/acsomega.2c07276
ACS Omega 2022, 7, 48583−48599

observed variations in $\iota_{em(p)}$ of the emitting ^{3}MLCT states of the Ru-bpy chromophores for $[Ru(bpy)_2(sc\text{-}CM)]^+$ and typical $[Ru(bpy)_{3-n}(Am)_{2n}]^{2+}$ complexes, a good linear relation with the intensity component values of ∑SOCM-IS was found, as seen in eq 3.[73] The photoinduced characteristics of $[Ru(bpy)_2(CM)]^+$ complexes with a bidentate π-aromatic-rich CM ligand (π_{Ar}-CM = diphenylpyrazine (dpz) and 1-phenylisoquinoline (piQ)) in this study are interesting because the observed absorption and photoinduced phosphorescence efficiencies ($\iota_{em(p)}$) are significantly different from those of $[Ru(bpy)_2(sc\text{-}CM)]^+$ complexes. The unusually higher $\iota_{em(p)}$ values for the $[Ru(bpy)_2(\pi_{Ar}\text{-}CM)]^+$ complexes compared to the corresponding values for the $[Ru(bpy)_2(sc\text{-}CM)]^+$ complexes are related to the fundamental principle (eqs 1−3) and the transition intensity perturbation, which is the focus of this investigation. Because studies such as these have been limited in the past, these data should contribute to the future development of and a better understanding of these types of theoretical frameworks. The skeletal structures of several of the ligands, the target $[Ru(bpy)_2(CM)]^+$ complexes (a−e) and reference $[Ru(bpy)_{3-n}(Am)_{2n}]^{2+}$ ions (1−5), are shown in Figure 2.

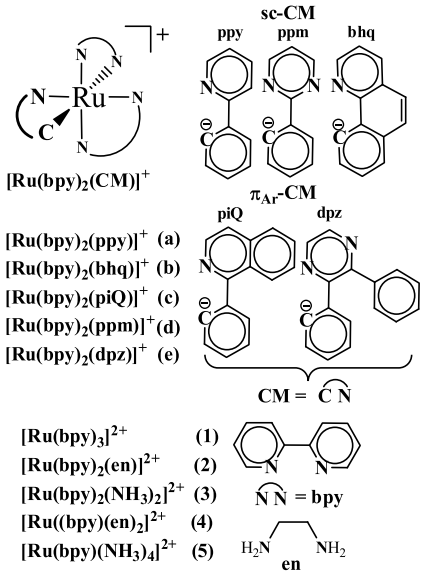

Figure 2. Skeletal structures of the $[Ru(bpy)_2(CM)]^+$ and reference $[Ru(bpy)_{3-n}(Am)_{2n}]^{2+}$ complexes, where Am = amine ligand and $2 \geq n \geq 0$.

EXPERIMENTAL SECTION

Details concerning the commercial starting materials, synthesis procedures, and nuclear magnetic resonance (NMR, ^{1}H and ^{13}C) spectral parameters of the target $[Ru(bpy)_2(CM)](PF_6)$ complexes are shown in Section S1A (page S2); the following compounds: $[Ru(bpy)_{3-n}(Am)_{2n}](PF_6)$ (1−5), $[Ru(bpy)_2(ppy)](PF_6)$ (a), $[Ru(bpy)_2(bhq)](PF_6)$ (b), and $[Ru(bpy)_2(piQ)](PF_6)$ (c) in Figure 2 were prepared as described in the literature.[84,89,94−96] Details regarding the X-ray structure determinations are provided in Section S1B (page S6), and the X-ray structure parameters of $[Ru(bpy)_2(dpz)](PF_6)\cdot(CH_2Cl_2)$ are shown in Figure S1B1 (page S7) and Tables S1B1 and S1B2 (pages S7−S9). Instrumentation details for the electrochemistry, room-temperature (RT) and 87 K absorption spectra, 77 K emission, lifetime measurements, and emission quantum yields ($\phi_{(em)}$) are provided in Section S1C (page S10). The electrochemical results, namely, the $E_{1/2}(Ru^{III/II})$ and $E_{1/2}(bpy^{0/-1})$ values, of the $[Ru(bpy)_2(CM)]^+$ ions are shown in Table S2A (page S12), and the photoinduced parameters obtained from experimental observations of the complexes are shown in Table 1 for $[Ru(bpy)_2(CM)]^+$ and Table S2B (page S13) for the reference $[Ru(bpy)_{3-n}(Am)_{2n}]^{2+}$ complexes. The 87 K absorption spectra of the $[Ru(bpy)_2(CM)]^+$ complexes in butyronitrile glasses are shown in Figure S2A (page S14). Computational results concerned about the density functional theory (DFT) modeling of the target complexes are shown in Section S3 (page S14). The DFT calculations performed in the present study used a combination of the B3PW91 functional[97−100] and the SDDall[101−103] basis set. We used several functionals to calculate the low-energy MLCT electronic absorption envelopes for $[Ru(bpy)_2(ppy)]^+$,[73] and we ultimately selected the B3PW91 functional for use in the present study; this method has been widely used to calculate absorption spectra of Ru-bpy chromophores that are analogous to the present systems.[8,9,73,104−107] DFT geometry optimizations for the S_0 and T_1 (T_e) states and time-dependent DFT (TDDFT) calculations for the electronic absorption spectra were performed in an acetonitrile solution simulated by the integral equation formalism polarizable continuum model (IEF-PCM) solvation model.[108−111] Harmonic vibrational frequency analyses were carried out to confirm that all of the optimized structures are minima on the potential energy surface. The electronic structures of the transitions were analyzed using the natural transition orbital (NTO) approach.[112,113] All calculations were performed using the Gaussian 09 program.[114]

Table 1. Ambient Absorption, 77 K Emission, Emission Decay Constants, and Emission Yield of the Complexes[a]

			77 K emission properties						
code	complex	$h\nu_{max}$ (abs), cm^{-1}/10^3, 87 K [298 K]	$h\nu_{max}$ (em), cm^{-1}/10^3	$h\nu_{ave}$, cm^{-1}/10^3	τ_{mean} (μs)	k_{obs}, μs^{-1}[b]	$\phi_{em} \times 10^3$	k_{RAD}, μs^{-1}[c]	k_{NRD}, μs^{-1}[d]
a	$[Ru(bpy)_2(ppy)]^+$[e]	18.1 [18.3]	13.48	12.57	3.38	2.96	17 ± 4	0.050 ± 0.009	2.9
b	$[Ru(bpy)_2(bhq)]^+$[e]	18.3 [18.5]	13.68	12.79	4.88	2.05	20 ± 4	0.041 ± 0.008	2.01
c	$[Ru(bpy)_2(piQ)]^+$[f]	18.7 (sh) [18.6]; 19.9 [19.8]	13.58	12.73	3.71	2.70	31 ± 6	0.084 ± 0.014	2.6
d	$[Ru(bpy)_2(ppm)]^+$[f]	18.5 [18.7]	13.86	13.02	5.71	1.75	28 ± 7	0.049 ± 0.012	1.7
e	$[Ru(bpy)_2(dpz)]^+$[f]	17.8 (sh) [18.1]; 20.3 [20.4]	13.97	13.14	5.39	1.86	46 ± 9	0.085 ± 0.017	1.8

[a]Dominant RT low-energy absorption maxima, $h\nu_{max}$(abs), determined in acetonitrile; emission maxima, $h\nu_{max}$ (em); average emission energy ($h\nu_{ave}$) by eq S1b (page S12), $\nu_{ave} \approx \int \nu_m I_m d\nu_m / \int I_m d\nu_m$; mean excited-state decay rate constant, $k_{obs} = 1/\tau_{mean}$, emission yield, ϕ_{em}, determined at 77 K in butyronitrile glasses, and sh = shoulder. [b]$k_{obs} = 1/\tau_{mean}$. [c]$k_{RAD} = \phi_{em} \times k_{obs}$. [d]$k_{NRD} = k_{obs} - k_{RAD}$. [e]Ref 73. [f]Spectral parameters in this work.

https://doi.org/10.1021/acsomega.2c07276
ACS Omega 2022, 7, 48583−48599

RESULTS

Experimental Observations. The 87 K absorption spectra of the target $[Ru(bpy)_2(CM)]^+$ (a−e) complexes are shown in Figure S2A (page S14), and the 298 K absorption spectra of the reference $[Ru(bpy)_{3-n}(Am)_{2n}]^{2+}$ (1, 2, and 4) and target $[Ru(bpy)_2(CM)]^+$ (a−e) complexes are shown in Figure 3. The intense low-energy single absorption bands of

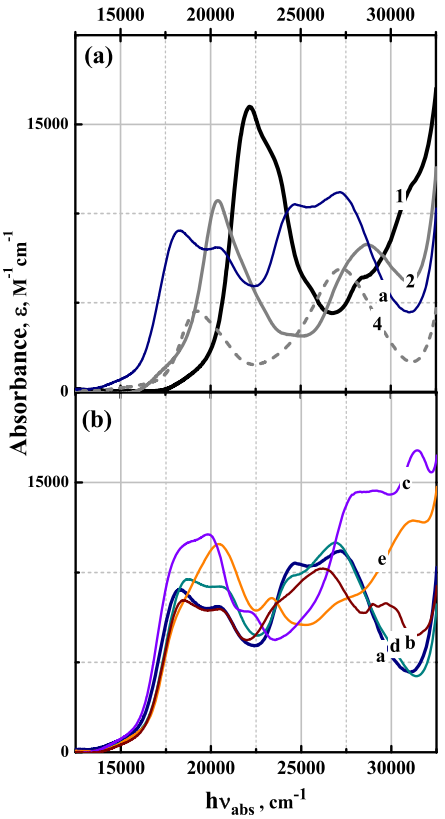

Figure 3. 298 K absorption spectra in CH_3CN for the reference complexes, top panel: $[Ru(bpy)_3]^{2+}$ (black solid, 1), $[Ru(bpy)_2(en)]^{2+}$ (gray solid, 2), $[Ru(bpy)(en)_2]^{2+}$ (gray dash, 4), and $[Ru(bpy)_2(ppy)]^+$ (dark blue solid in the top and bottom panels, a); 298 K absorption spectra in CH_3CN for target complexes, solid curves in the lower panel: $[Ru(bpy)_2(bhq)]^+$ (wine, b), $[Ru(bpy)_2(piQ)]^+$ (violet, c), $[Ru(bpy)_2(ppm)]^+$ (green, d), and $[Ru(bpy)_2(dpz)]^+$ (orange, e). The complex codes are shown in Figure 2.

the three reference complexes in Figure 3 are attributed to the sum of the primary ^{1}MLCT excited states of the Ru-bpy chromophore.[1,2,65,115,116] Furthermore, the broad low-energy absorption bands (15,000−22,500 cm^{-1}, 660−440 nm) of the $[Ru(bpy)_2(sc\text{-}CM)]^+$ ions (sc-CM = ppy (a) and bhq (b)) are attributed to the sum of the intensities of ^{1}MLCT excited states of two nonidentical Ru-bpy moieties,[73,84,117] and the shapes of the low-energy absorption bands for the sc-CM = ppm complex in this region are similar to those of the sc-CM = ppy and bhq complexes. The shapes of the low-energy bands in the 298 and 87 K absorption spectra for $[Ru(bpy)_2(\pi_{Ar}\text{-}CM)]^+$ (CM = piQ (c) and dpz (e)) are different from those of the $[Ru(bpy)_2(sc\text{-}CM)]^+$ ions, and the results of DFT modeling suggest that the first low-energy band in the spectra of the $[Ru(bpy)_2(\pi_{Ar}\text{-}CM)]^+$ complexes includes intense contributions from the ^{1}MLCT excited states of the Ru-bpy and Ru-CM moieties. The nonidentical absorption curves in the high-energy region (22,500−30,000 cm^{-1}, 440−333 nm) imply that the absorption transition behaviors for the $[Ru(bpy)_2(CM)]^+$ complex series are very different in this work.

The 77 K ^{3}MLCT phosphorescence bands in the spectra of the $[Ru(bpy)_2(ppy)]^+$ (a) and target reference $[Ru(bpy)_3]^{2+}$ (1), $[Ru(bpy)_2(en)]^{2+}$ (2), and $[Ru(bpy)(en)_2]^{2+}$ (4) ions in the top panel of Figure 4 show recognizable vibronic side

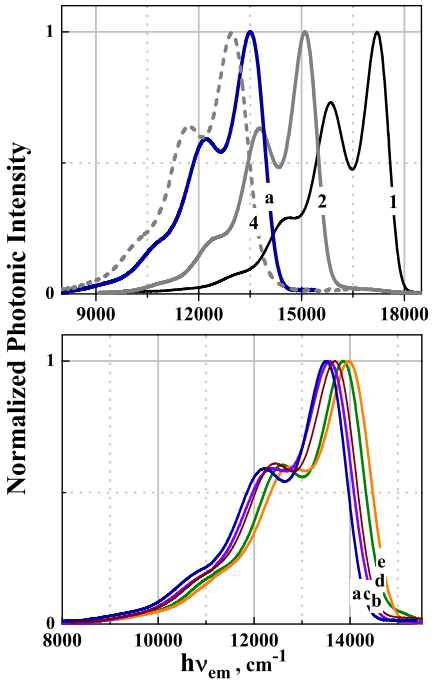

Figure 4. 77 K phosphorescence spectra in butyronitrile glasses of the reference $[Ru(bpy)_{3-n}(Am)_{2n}]^{2+}$ and target $[Ru(bpy)_2(CM)]^+$ complexes. The complex codes are shown in Figure 2.

bands corresponding to ^{3}MLCT Ru-bpy chromophores, which is attributed to the identified vibronic characteristics of MLCT Ru-bpy chromophores.[65,73,84,95,116,118−122] The 77 K emission spectra of the $[Ru(bpy)_2(CM)]^+$ (a−e) complexes in Figure 4 are attributed to the ^{3}MLCT emitting state (T_e) of a typical Ru-bpy chromophore such as the reference $[Ru(bpy)_{3-n}(Am)_{2n}]^{2+}$ (1−5),[73,84] and the observed k_{NRD} vs the emission energy scale (Figure 5) and a DFT natural transition orbital (NTO) plot of the triplet emitting state (T_e) provided in the section described in the Computational Results further illustrate this point.

In principle, the k_{NRD} (ambient temperature) of the emitting ^{3}MLCT excited state of Ru-diimine complexes can be attributed to the ^{3}MLCT → ^{3}MC internal conversion (k_{IC}),[7] but we have no evidence for this assumption from the 77 K k_{NRD} observations of the Ru-bpy chromophores of the $[Ru(bpy)_2(sc\text{-}CM)]^+$ (a, b, and d) complexes.[73,84] The 77 K k_{NRD} relaxation of the lowest-energy ^{3}MLCT-(Ru-bpy) excited state for the typical $[Ru(bpy)_{3-n}(Am)_{2n}]^{2+}$ series would be expected to involve only an argument of k_{NRD} (^{3}MLCT → S_0) ≫ k_{IC} (^{3}MLCT → ^{3}MC).[65,95,106,121] Furthermore, the 77 K k_{NRD} values for the different chromophores can be expressed in terms of a temperature-independent k_{NRD} formalism based on a single-distortion model, $h\nu_k$,[12,44]

$$\ln k_{NRD} \approx \ln[B(H_{e,g})^2] - \gamma_{Ek}(E_{em}/h\nu_k) \quad (4)$$

where $B \approx [8\pi^3/(h^3\nu_k h\nu_{ave})]^{1/2}$ and $\gamma_{Ek} \approx [\ln(E_{em}/\lambda_k) - 1]$, in which we substituted $h\nu_{ave}$ for E_{em} in eq 4, and the $h\nu_{ave}$ scale

https://doi.org/10.1021/acsomega.2c07276
ACS Omega 2022, 7, 48583−48599

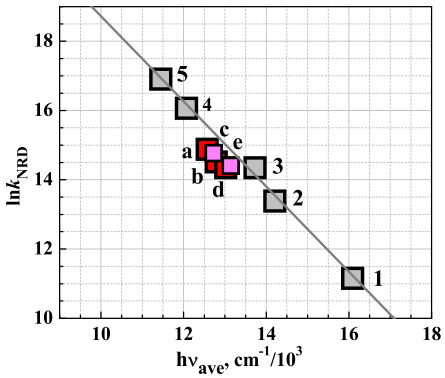

Figure 5. Comparison of the variations in k_{NRD} with emission $h\nu_{ave}$ for the complexes shown in Table 1 and Table S2B (page S13). Gray squares denote the reference $[Ru(bpy)_{3-n}(Am)_{2n}]^{2+}$ series, and red squares (L_{Ar} = sc-CM: ppy (a), bhq (b), and ppm (d)) and pink squares (L_{Ar} = π_{Ar}-CM: piQ (c) and dpz (e)) denote $[Ru(bpy)_2(L_{Ar})]^+$ complexes. The gray solid least-squares line of the $[Ru(bpy)_{3-n}(Am)_{2n}]^{2+}$ complexes is drawn with a slope of −0.00123 ± 0.00005, an intercept of 31.0 ± 0.6, and an R^2 value of 0.99.

in Figure 5 is associated with the $h\nu_{ave}/h\nu_k$ scale; $H_{e,g}$ is a function of SOC; the distorted ν_k frequency in the equation is related to an active distortion mode of the harmonic model whose energy approximates those of the excited state, $jh\nu_k \approx h\nu_{ave}$; λ_k is obtained from the Huang−Rhys parameter for this ν_k mode.[116,123] The k_{NRD} value of the $[Ru(bpy)_2(CM)]^+$ complexes is similar to the least-squares fit of the reference $[Ru(bpy)_{3-n}(Am)_{2n}]^{2+}$ series in the given emission energy region, and this finding provides empirical evidence in support for the intrinsic characteristic of the ^{3}MLCT-(Ru-bpy) emitting states (T_e) of both series of complexes.[73,84]

A plot of the observed phosphorescence efficiency ($\iota_{em(p)}$) versus emission energy ($h\nu_{ave}$) for the $[Ru(bpy)_2(CM)]^+$ and the typical $[Ru(bpy)_{3-n}(Am)_{2n}]^{2+}$ series complexes is shown in Figure 6. The 77 K emission quantum yields (ϕ_{em}) for the $[Ru(bpy)_2(CM)]^+$ complexes are in the range within 1−5%, and the $\iota_{em(p)}$ amplitudes of the $[Ru(bpy)_2(sc\text{-}CM)]^+$ complexes are approximately twofold higher than those of the typical $[Ru(bpy)_{3-n}(Am)_{2n}]^{2+}$ series (for sc-CM = ppy, bhq,[73] and ppm); in addition, the outstanding $\iota_{em(p)}$ values of the $[Ru(bpy)_2(\pi_{Ar}\text{-}CM)]^+$ complexes (π_{Ar}-CM = piQ and dpz)

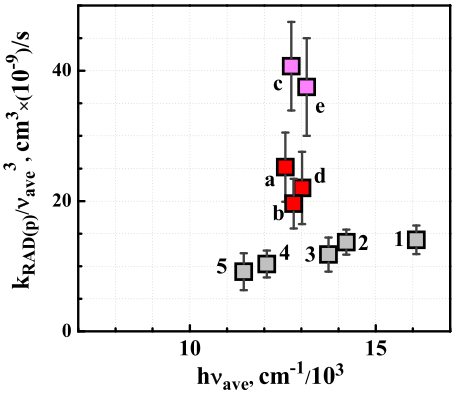

Figure 6. Comparison of the variations in $\iota_{em(p)} = k_{RAD(p)}/(\nu_{ave})^3$ with $h\nu_{ave}$ for the complexes: gray squares denote the reference $[Ru(bpy)_{3-n}(Am)_{2n}]^{2+}$ series, red squares denote the $[Ru(bpy)_2(sc\text{-}CM)]^+$ complexes, and pink squares denote the $[Ru(bpy)_2(\pi_{Ar}\text{-}CM)]^+$ complexes.

are nearly fourfold higher than those of the reference Ru-bpy complexes, i.e., nearly twofold higher than those of the $[Ru(bpy)_2(sc\text{-}CM)]^+$ complexes at the given energy. These unusually high $\iota_{em(p)}$ amplitudes for the $[Ru(bpy)_2(\pi_{Ar}\text{-}CM)]^+$ complexes are likely derived from the fundamental relations of $\iota_{em(p)}$ and ∑SOCM-IS, based on eq 3.

Computational Results. The TDDFT-calculated low-energy $S_{n(X)}$ excited-state (X = S and T at S_0 and T_1 geometries, respectively) parameters, their configurations of the highest occupied molecular orbitals (HOMOs) and the lowest unoccupied molecular orbitals (LUMOs), and orbital plots of the HOMOs and LUMOs for the $[Ru(bpy)_2(CM)]^+$ (CM = ppm, piQ, and dpz) ions are shown in Tables S3A1−A3 and Figures S3A1−A3 (pages S15−S19). The DFT model of the target complexes indicates that the first three HOMOs have $d\pi_{\parallel}$ ($d\pi$-Ru in HOMO) and two $d\pi_{\perp}$ ($d\pi$-Ru in HOMO-1 and HOMO-2) orbital characteristics and that the first three LUMOs have π^*-bpy (LUMO and LUMO+1) and π^*-CM (LUMO+2) characteristics. The TDDFT parameters and NTO plots of $S_{n(X)}$ and T_n for the target Ru-CM complexes are also shown in Tables S3B1−B3 and Figures SC1−C3 (pages S21−S50), and the donor-NTO component in each low-energy $S_{n(X)}$ excited state is the primary HOMO ($d\pi_{\parallel}$), HOMO-1 ($d\pi_{\perp a}$), or HOMO-2 ($d\pi_{\perp b}$), see Tables S3A1−A3 and Figures S3A1−A3 (pages S15−S19); the notations of the correlation $d\pi$ orbital are shown in Figure S6B (page S89). Comparisons of the RT-observed and DFT-calculated absorption transitions of the target Ru-CM complexes are shown in Figure 7 and Figure S3B1 (page S20). In the DFT modeling of the $[Ru(bpy)_2(CM)]^+$ (CM = ppy) ion in our previous report[73] and the target $[Ru(bpy)_2(CM)]^+$ (CM = ppm, piQ, and dpz) ions reported here, the notation for the calculated oscillator strength of singlet transitions (lo-*f*, 0.005 > *f*; m-*f*, 0.05 > *f* > 0.005; and h-*f*, *f* > 0.05) was applied in the present text.

Since the phosphorescence of a complex is fundamentally a spin-forbidden transition, the values for the phosphorescence efficiency, $\iota_{em(p)}$, of the emitting state in the formalism of eq 3 should depend on the sum of the SOCM-IS (∑SOCM-IS) intensity from the efficient low-energy singlet excited states ($S_{n(T)}$) in a T_e geometry. The difference in low-energy absorption band shapes between the $[Ru(bpy)_2(sc\text{-}CM)]^+$- and $[Ru(bpy)_2(\pi_{Ar}\text{-}CM)]^+$-type ions in Figure 3 indicates the different MLCT compositions of their low-energy $S_{n(S)}$ states. Based on these observations and the DFT modeling of the $[Ru(bpy)_2(sc\text{-}CM)]^+$ ions (sc-CM = ppy[73] and ppm), the observed similarities in the absorption band shapes of the complexes are attributed to the similar intensities and energies of the low-energy intense-$S_{n(S)}$ states. The calculated absorption results for both ions indicate that their observed first lowest-energy absorption band (14,000−22,500 cm^{-1}) is the highest of the MLCT-(Ru-bpy)-type $S_{n(S)}$ intensity contribution and includes the intense $S_{5(S)}$ (h-*f*) and $S_{6(S)}$ (h-*f*) for $[Ru(bpy)_2(ppy)]^+$ and $S_{5(S)}$ (h-*f*) and $S_{7(S)}$ (h-*f*) for $[Ru(bpy)_2(ppm)]^+$. Furthermore, the first MLCT-(Ru-CM)-type $S_{n(S)}$ state has contributions from $S_{7(S)}$ (lo-*f*) for $[Ru(bpy)_2(ppy)]^+$ and $S_{6(S)}$ (lo-*f*) for $[Ru(bpy)_2(ppm)]^+$. For both $[Ru(bpy)_2(sc\text{-}CM)]^+$ complexes, the second low-energy band (22,500−30,000 cm^{-1}) includes MLCT-(Ru-bpy) and MLCT-(Ru-CM) transitions. In addition, the major absorption bands in the high-energy region (>33,000 cm^{-1}) are attributed to intraligand $\pi\pi^*$ (intra-$\pi\pi^*$) and interligand $\pi\pi^*$ (inter-$\pi\pi^*$) transitions. The shapes of the DFT-calculated

https://doi.org/10.1021/acsomega.2c07276
ACS Omega 2022, 7, 48583−48599

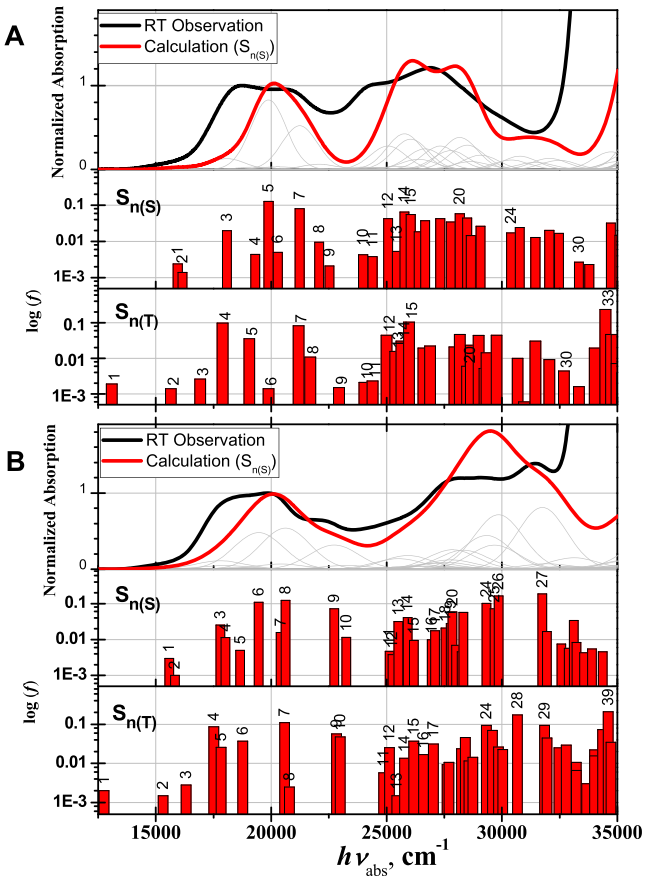

Figure 7. Illustrations of the observed RT absorption (black curve) and DFT (B3PW91)-calculated absorptions (red curve, S_0 geometry) and oscillator strengths (f) of the $S_{n(X)}$ transitions (X = S and T for singlet and triplet excited states, respectively) of selected complexes are shown in panel (A) ($[Ru(bpy)_2(ppm)]^+$) and panel (B) ($[Ru(bpy)_2(piQ)]^+$). The log(f) values of the low-energy $S_0 \rightarrow S_n$ transitions for each complex are plotted in the S_0 geometry ($S_{n(S)}$, central) and in the T_e geometry ($S_{n(T)}$, bottom).

absorption band for the $[Ru(bpy)_2(\pi_{Ar}\text{-CM})]^+$-type ions indicate that the first low-energy absorption band (14,000–25,000 cm^{-1}) can be attributed to the contribution of the intensity from the MLCT excited states of both Ru-bpy- and Ru-CM-type chromophores including (1) intense $S_{6(S)}$ (h-f, Ru-bpy), $S_{8(S)}$ (h-f, configurational Ru-bpy and Ru-CM), and $S_{9(S)}$ (h-f, configurational Ru-bpy and Ru-CM) components for $[Ru(bpy)_2(piQ)]^+$ and (2) intense $S_{6(S)}$ (h-f, Ru-bpy) and $S_{8(S)}$ (h-f, configurational Ru-bpy and Ru-CM) components for $[Ru(bpy)_2(dpz)]^+$. In addition, the first MLCT-(Ru-CM)-type $S_{n(S)}$ state is presented in $S_{4(S)}$ (m-f) for $[Ru(bpy)_2(piQ)]^+$ and $S_{4(S)}$ (lo-f) for $[Ru(bpy)_2(dpz)]^+$. Furthermore, the absorption for both $[Ru(bpy)_2(\pi_{Ar}\text{-CM})]^+$ complexes in the 25,000–33,000 cm^{-1} region includes MLCT-(Ru-bpy), MLCT-(Ru-CM), intra-$\pi\pi^*$ and inter-$\pi\pi^*$ transitions, and the absorption in the high-energy region (>33,000 cm^{-1}) is attributed to intra-$\pi\pi^*$ and inter-$\pi\pi^*$ transitions. Moreover, $S_{16(S)}/S_{17(S)}$ (m-f) for $[Ru(bpy)_2(piQ)]^+$ and $S_{19(S)}/S_{20(S)}$ (m-f) for $[Ru(bpy)_2(dpz)]^+$, corresponding to the first inter-$\pi\pi^*$-type transition, occur at a lower energy than that for the $[Ru(bpy)_2(sc\text{-}CM)]^+$ ions. The NTO plots and the orbital compositions of the low-energy $S_{n(S)}$ excited states of the target $[Ru(bpy)_2(CM)]^+$ ions are shown in Figures S3C1A–C3A (pages S27–S30, S35–S38, and S42–S45) and Table S5A (page S69).

The calculated parameters for the $S_{n(T)}$ (in the T_e geometry) excited states and the NTO plots for the $[Ru(bpy)_2(CM)]^+$ ions in this work were used for the ∑SOCM-IS formalism (eq 3) in the Discussion section, and no significant difference between the calculated results for the $S_{n(S)}$ and $S_{n(T)}$ states was found for each ion; see Tables S3B1–B3 (pages S21–S26) and Figures S3C1A and S3C1B (pages S27–S33) for $[Ru(bpy)_2(ppm)]^+$, Figures S3C2A and S3C2B (pages S35–S40) for $[Ru(bpy)_2(piQ)]^+$, Figures S3C3A and S3C3B (pages S42–S49) for $[Ru(bpy)_2(dpz)]^+$, and our previous work[73] concerning $[Ru(bpy)_2(ppy)]^+$. The NTOs-$S_{n(T)}$ compositions of the target complexes should be examined carefully because the phosphorescence efficiencies depend on the ΣSOCM-IS values of the $S_{n(T)}$ excited states; the detailed orbital configurations for the $S_{n(T)}$ states of the $[Ru(bpy)_2(CM)]^+$ ions are shown in Table S5B (page S71), and more concise results are provided in the Discussion section.

Previous work concerning the DFT modeling of the emitting ^{3}MLCT (T_e) states for typical Ru-bpy complexes predominantly involved MLCT-(Ru-bpy) and some $\pi\pi^*$-bpy components for $[Ru(bpy)(NH_3)_4]^{2+}$,[8,65,73,106] $[Ru(bpy)(en)_2]^{2+}$,[107] and $[Ru(bpy)_2(en)]^{2+}$[65,73] complexes. The selected low-energy NTO plots of the triplet excited states (T_n) with excited-state energies at the T_e geometry for the target $[Ru(bpy)_2(CM)]^+$ ions are shown in Figures S3C1C (page S34), S3C2C (page S41), and S3C3C (page S50). The NTOs of the emitting T_e (T_1) states of $[Ru(bpy)_2(CM)]^+$ with T_e coordinates (Figure 8) show donor orbital configurations that are composed primarily of the dπ-Ru component with some contribution from the pπ-CM (for most phenyl groups) and pπ-$bpy_{(b)}$ moieties and the acceptor orbital, possessing mostly pπ^*-$bpy_{(b)}$ characteristics. We also calculated the Mulliken spin density (SD) values for the T_e excited states at the Ru centers and on the CM and $bpy_{(b)}$ moieties for the $[Ru(bpy)_2(CM)]^+$ series (see Figure 8), and the results show that most of the SD populations of the T_e states are localized on the Ru-$bpy_{(b)}$ moiety. These results indicate that the emitting T_e excited states of the target $[Ru(bpy)_2(CM)]^+$ complexes primarily have ^{3}MLCT-(Ru-bpy) characteristics.

From these results, the following conclusions can be drawn: (a) The lowest-energy absorption band of the $[Ru(bpy)_2(CM)]^+$ complexes has a typical MLCT band shape with two observed maxima corresponding to CM = ppy, bhq, and ppm (sc-CM) and an intense, broad band for CM = piQ and dpz (π_{Ar}-CM). (b) The observed shape of the 77 K emission and the k_{NRD} amplitudes in the given energy of the target $[Ru(bpy)_2(CM)]^+$ complexes indicate the ^{3}MLCT characteristics of the Ru-bpy chromophore.[73] (c) The phosphorescence efficiency ($\iota_{em(p)}$) of the target $[Ru(bpy)_2(CM)]^+$ complexes at the specified energy is approximately twofold (for CM = sc-CM) and fourfold (CM = π_{Ar}-CM) higher on average than those of the typical reference $[Ru(bpy)_{3-n}(Am)_{2n}]^{2+}$ ions. (d) DFT modeling of the $[Ru(bpy)_2(CM)]^+$ complexes in their ground-state geometries (S_0) indicates that the intensity of the low-energy absorption band has contributions primarily from the MLCT(Ru-bpy)-type excited states for the CM = sc-CM-type complexes, as well as from both efficient MLCT(Ru-bpy)- and MLCT(Ru-CM)-type excited states for the CM = π_{Ar}-CM-type complexes. The high-energy absorption bands of the $[Ru(bpy)_2(CM)]^+$ complexes reported in this work include contributions from

https://doi.org/10.1021/acsomega.2c07276
ACS Omega 2022, 7, 48583–48599

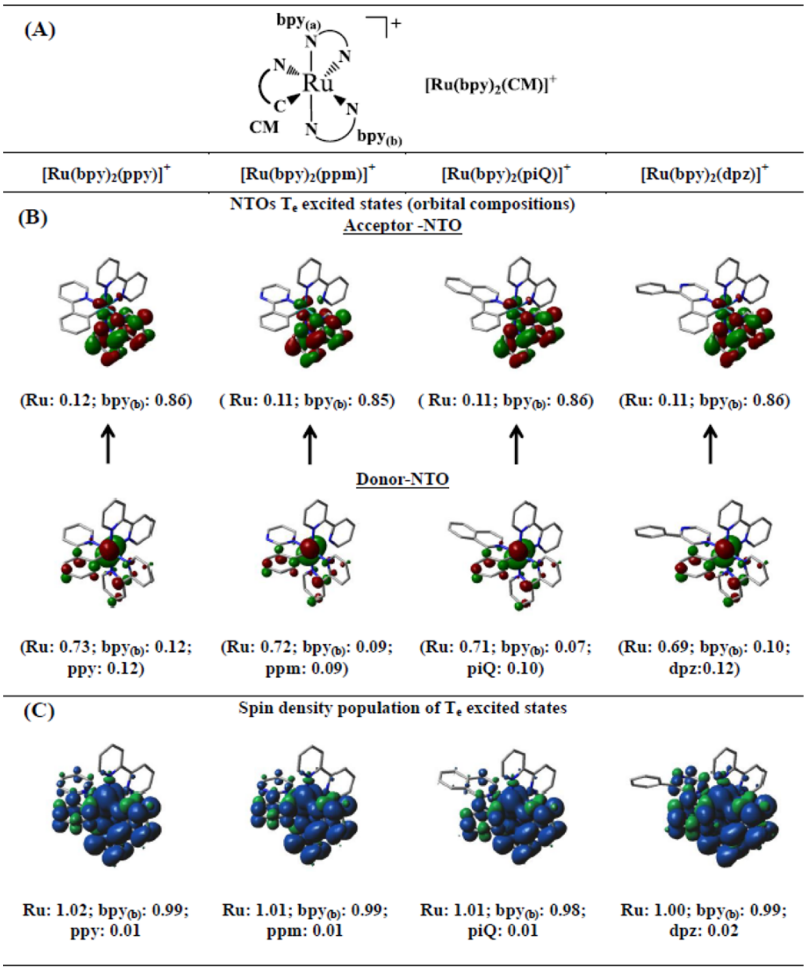

Figure 8. DFT results with the T_e coordinates for the $[Ru(bpy)_2(CM)]^+$ ion: (a) illustrated moiety symbols for the Δ-form target complexes in panel (A) (top); (b) Mulliken orbital population analyses for the NTOs, including donor and acceptor NTOs (central panel (B)) and the calculated spin density composition (SD, bottom panel (C)) of the T_e (T_1) excited state for the Ru center and the CM and $bpy_{(b)}$ moieties for each ion.

the MLCT-type Ru-bpy and Ru-CM excited states and $\pi\pi^*$-type intraligand and interligand excited states. (e) DFT modeling of the NTOs and SD plots of the T_e (T_1) state for each target $[Ru(bpy)_2(CM)]^+$ ion shows mostly MLCT-(Ru-bpy)-type characteristics.

DISCUSSION

In a real complex system, the $\iota_{em(p)}$ determined from eq 3 should be obtained from the phosphorescence parameters (see Table 1), and the transition moment term $(M_{S_{n(T)},S_0})$ in eq 3 is an oscillator-strength (f) function of the singlet excited state with T_e coordinates:[12]

$$f_{S_{n(T)},S_0} = \frac{8\pi^2 m_e \nu_{S_{n(T)},S_0}}{3e^2h}(M_{S_{n(T)},S_0})^2 = C_f \nu_{S_{n(T)},S_0}(M_{S_{n(T)},S_0})^2$$

$$\Rightarrow (M_{S_{n(T)},S_0}) = \sqrt{\frac{1}{C_f} \times \frac{f_{S_{n(T)},S_0}}{\nu_{S_{n(T)},S_0}}} \quad (5)$$

where $1/C_f = 3e^2h/8\pi^2 m_e$, m_e is the mass of an electron, and $\nu_{S_{n(T)},S_0}$ corresponds to the emission energy of $S_{n(T)} \rightarrow S_0$.

The results of DFT modeling suggest a low calculated reorganization energy ($\lambda_{reg(T)} \approx 1590 \pm 20$ cm^{-1}; see the definition in Figure S5A, page S68) for the light ground-state distortion in the T_e geometry of the target complexes. The oscillator strength in eq 5 can fundamentally be described by a Gaussian curve (see eq S4m, page S56), but attention needs to be paid to the fundamental quality of the detailed derivation regarding the $f_{S_{n(T)},S_0}$ term in eq 5 from the absorption parameters of a complex system with a postulated light ground-state distortion at a T_e geometry. The energy-weighted intensity stealing term, the SOC-mediated energy-weighted absorptivity (SOCEWA),[73] instead of $f_{S_{n(T)},S_0}$, can then be obtained from the observed absorption parameters; see eqs S4r–S4t (pages S57–S58). The $\iota_{em(p)}$ equation containing the integration of the SOCEWA value ($\int$SOCEWA $d\nu = \int\left[\left(\frac{\varepsilon_i(\nu_i)}{W_i(\nu_i)}\right)\right] d\nu$) is related to the absorption spectrum through[73]

$$\iota_{em(p)} \equiv \frac{k_{RAD(p)}}{(\nu_{T_e,S_0})^3} \approx C_{RAD(p)}(H^{SOC}_{T_e,S_{n(T)}})^2 \int\left[\left(\frac{\varepsilon_i(\nu_i)}{W_i(\nu_i)}\right)\right] d\nu \quad (6)$$

https://doi.org/10.1021/acsomega.2c07276
ACS Omega 2022, 7, 48583−48599

where $\varepsilon_i(\nu_i)$ is the observed absorptivity at ν_i, $W_i(\nu_i) = (E_{T_e} - \nu_i)^2\nu_i$, and $C_{RAD(p)} = (8.60 \times 10^{-9})(g_{T_e}/g_{S_n})$, where g is a multiplicity weighting factor. The derivation of eq 6 is shown in Section S4B (pages S57−S60). The procedures used for the fitting and parameters for the $\int$SOCEWA dν values from the experimental 87 K low-energy absorption curve of the complexes are shown in Figure S4D2 (page S62) and Table S4 (page S65).

The slope of the plot of $\iota_{em(p)}$ versus $\int$SOCEWA dν for the typical $[Ru(bpy)_{3-n}(Am)_{2n}]^{2+}$ and plain $[Ru(bpy)_2(CM)]^+$ complex series suggests that $H^{SOC} \approx 100$ cm^{-1} for the Ru-bpy chromophore.[73] A plot of $\iota_{em(p)}$ versus $\int$SOCEWA dν for the target complexes prepared in this work is presented in Figure 9, and the slope of the least-squares line containing the

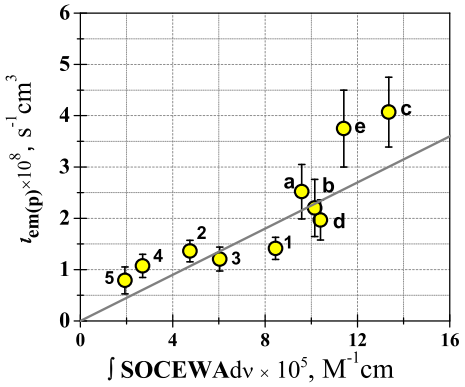

Figure 9. Illustration of the $\iota_{em(p)}$ $(k_{RAD(p)}/(\nu_{ave})^3)$ dependencies on the integrated SOCEWA ($\int$SOCEWA dν), based on eq 6, for several Ru-bpy chromophores: $[Ru(bpy)_2(CM)]^+$, a−e codes in Figure 1; $[Ru(bpy)_3]^{2+}$, 1; $[Ru(bpy)_2(en)]^{2+}$, 2; $[Ru(bpy)_2(NH_3)_2]^{2+}$, 3; $[Ru(bpy)(en)_2]^{2+}$, 4; $[Ru(bpy)(NH_3)_4]^{2+}$, 5. The least-squares line including the target complexes (1−5 and $[Ru(bpy)_2(sc\text{-}CM)]^+$ complexes; a, b, and d), with $R^2 = 0.92$ and slope = $(2.25 \pm 0.14) \times 10^{-4}$. The $\int$SOCEWA dν parameters of the complexes are shown in Table S4 (page S65).

typical $[Ru(bpy)_{3-n}(Am)_{2n}]^{2+}$ ions and $[Ru(bpy)_2(sc\text{-}CM)]^+$ complexes (CM = ppy, bhq, and ppm) also suggests a similar result of $H^{SOC} \approx 100$ cm^{-1} for the Ru-bpy chromophore, where $C_{RAD(p)} = (8.60 \times 10^{-9})(g_{T_e}/g_{S_n})$ and $g_{T_e}/g_{S_n} = 3$ (see eq S4t, page S58). The least-squares line in Figure 9 appears idealized by eq 6, but the issue of why the $\iota_{em(p)}$ values of $[Ru(bpy)_2(\pi_{Ar}\text{-}CM)]^+$ (π_{Ar}-CM = piQ (c) and dpz (e)) are approximately 1.4−1.5-fold greater than those along the least-squares line in the given $\int$SOCEWA dν region is interesting.

Definition of Donor and Acceptor Orbital Types Leading to SOC Configurational Mixing between the $S_{n(T)}$ and T_e States. Since the significantly high $\iota_{em(p)}$ amplitudes of the $[Ru(bpy)_2(\pi_{Ar}\text{-}CM)]^+$ complexes (π_{Ar}-CM = piQ and dpz) in Figure 9 cannot be explained by a simple relationship between the $\iota_{em(p)}$ values and the components of $\sum$SOCM-IS (by simply observing the $\int$SOCEWA dν value) in this work, we needed to return to the fundamental core for this consequence. The simple model of an excited state in a photoinduced transition includes donor and acceptor SOMOs (ϕ_D, D = donor, and ϕ_A, A = acceptor), i.e., $S_n = \phi_{D(S_n)}\phi_{A(S_n)}$ and $T_e = \phi_{D(T_e)}\phi_{A(T_e)}$; ϕ_D and ϕ_A in an MLCT excited state are the metal-dπ and L_{Ar}-pπ* bases, respectively; the spin−orbit operator in eq 2 can be expanded as $\hat{H}^{SO} = \hat{H}_D^{SO} + \hat{H}_A^{SO}$ for donor and acceptor orbital operations; H_{T_e,S_n}^{SOC} in eq 2 can be given by

$$H_{T_e,S_n}^{SOC} = \langle\phi_{D(S_n)}\phi_{A(S_n)}|\hat{H}_D^{SO} + \hat{H}_A^{SO}|\phi_{D(T_e)}\phi_{A(T_e)}\rangle$$
$$= \langle\phi_{D(S_n)}|\hat{H}_D^{SO}|\phi_{D(T_e)}\rangle\langle\phi_{A(S_n)}\phi_{A(T_e)}\rangle + \langle\phi_{D(S_n)}\phi_{D(T_e)}\rangle\langle\phi_{A(S_n)}|\hat{H}_A^{SO}|\phi_{A(T_e)}\rangle \quad (7)$$

The two conditions in eq 7 are attributed to the absence of SOC configurational mixing (type n) between the T_e and $S_{n(T)}$ states, $\phi_{D(S_n)} = \phi_{D(T_e)}$ with $\phi_{A(S_n)} = \phi_{A(T_e)}$ and $\phi_{D(S_n)} \neq \phi_{D(T_e)}$ with $\phi_{A(S_n)} \neq \phi_{A(T_e)}$, and these show both $\langle\phi_{D(S_n)}|\hat{H}_D^{SO}|\phi_{D(T_e)}\rangle\langle\phi_{A(S_n)}\phi_{A(T_e)}\rangle = 0$ and $\langle\phi_{D(S_n)}\phi_{D(T_e)}\rangle\langle\phi_{A(S_n)}|\hat{H}_A^{SO}|\phi_{A(T_e)}\rangle = 0$, i.e., $H_{T_e,S_n}^{SOC} = 0$ in eq 7.

Two idealized conditions in eq 7 show the logical SOC mixing in the following formalism:

1. If $\phi_{D(S_n)} \neq \phi_{D(T_e)}$ and $\phi_{A(S_n)} = \phi_{A(T_e)}$, then $\langle\phi_{D(S_n)}\phi_{D(T_e)}\rangle = 0$ and $\langle\phi_{A(S_n)}\phi_{A(T_e)}\rangle = 1$, and then, $\langle\phi_{D(S_n)}|\hat{H}_D^{SO}|\phi_{D(T_e)}\rangle = H_{D(T_e,S_n)}^{SOC} > 0$ and $\langle\phi_{A(S_n)}|\hat{H}_A^{SO}|\phi_{A(T_e)}\rangle = 0$ in eq 7; thus, $\langle\phi_{D(S_n)}|\hat{H}_D^{SO}|\phi_{D(T_e)}\rangle\langle\phi_{A(S_n)}\phi_{A(T_e)}\rangle = H_{D(T_e,S_n)}^{SOC}$ and $\langle\phi_{D(S_n)}\phi_{D(T_e)}\rangle\langle\phi_{A(S_n)}|\hat{H}_A^{SO}|\phi_{A(T_e)}\rangle = 0$. Then, eq 7 can be simplified to $H_{T_e,S_n}^{SOC} \approx H_{D(T_e,S_n)}^{SOC}$, which is attributed to donor SOMO-driven SOC configurational mixing (type D^{SOC}).
2. (2) If $\phi_{D(S_n)} = \phi_{D(T_e)}$ and $\phi_{A(S_n)} \neq \phi_{A(T_e)}$, then $\langle\phi_{D(S_n)}\phi_{D(T_e)}\rangle = 1$, $\langle\phi_{A(S_n)}\phi_{A(T_e)}\rangle = 0$, $\langle\phi_{D(S_n)}|\hat{H}_D^{SO}|\phi_{D(T_e)}\rangle = 0$, and $\langle\phi_{A(S_n)}|\hat{H}_A^{SO}|\phi_{A(T_e)}\rangle = H_{A(T_e,S_n)}^{SOC} > 0$ in eq 7, and then, $\langle\phi_{D(S_n)}|\hat{H}_D^{SO}|\phi_{D(T_e)}\rangle\langle\phi_{A(S_n)}\phi_{A(T_e)}\rangle = 0$ and $\langle\phi_{D(S_n)}\phi_{D(T_e)}\rangle\langle\phi_{A(S_n)}|\hat{H}_A^{SO}|\phi_{A(T_e)}\rangle = H_{A(T_e,S_n)}^{SOC}$; thus, eq 7 can be expressed as $H_{T_e,S_n}^{SOC} \approx H_{A(T_e,S_n)}^{SOC}$, which is considered to be the acceptor SOMO-driven SOC configurational mixing (type A^{SOC}).

It is also assumed that an $S_{n(T)}$ state contains more than one component, such as $S_{n(T)} = aS_{n(I)(T)} + bS_{n(II)(T)}$, where $a + b \approx 1$ $(0.25 < a/b < 4)$, in the $S_{4(T)}$ and $S_{5(T)}$ states of the $[Ru(bpy)_2(piQ)]^+$ ion (see the selected NTO plots in the next section; also see Figure S3C2B, pages S39−S40). Moreover, the significant relationship between both the $S_{n(X)(T)}$ components (X = I or II) of $S_{n(T)}$ and the T_e states in eq 7 are attributed to the D^{SOC}- and A^{SOC}-type-driven SOC configurations, respectively. Consequently, this $S_{n(T)}$ excited state is considered to contain both characters of D^{SOC}- and A^{SOC}-type SOC configurations with the T_e state, an $(A + D)^{SOC}$-type-driven form. The formula derivation (eq 7) and its detailed description can be found in the S4 section (pages S52−S54).

Evaluation of the Transition Moment Amplitude in the Phosphorescence Efficiency Formalism ($\iota_{em(p)}$) by SOC-Mediated Singlet Excited-State Intensity Based on the SOC Principle and DFT Modeling of the Complexes. *The Energy-Weighted Oscillator Strength in the $\sum$SOCM-IS Formalism.* To identify the relationship between the $\iota_{em(p)}$ value and the efficient $M_{S_{n(T)},S_0}$ contribution of a complex system, a quick plot of $\iota_{em(p)}$ versus $\int$SOCEWA dν on the low-temperature experimental observations of the target complexes, as shown in Figure 9, is a plausible relation for the target

https://doi.org/10.1021/acsomega.2c07276
ACS Omega 2022, 7, 48583−48599

complexes but cannot explain the significantly high $\iota_{em(p)}$ values of $[Ru(bpy)_2(\pi_{Ar}\text{-CM})]^+$ ions at the given $\int$SOCEWA $d\nu$. Because it is difficult to obtain the oscillator-strength value of each singlet excited state from the MLCT band of the experimental absorption spectra of the Ru(II)-L_{AR}-type complexes, an appropriate parameter from DFT modeling would be expected to assist in the formalism of eq 5. If the different singlet transition moments are approximately orthogonal for simplicity, i.e., $\vec{M}_{S_{n(MLCTx,\,T)},\,S_0} \cdot \vec{M}_{S_{n(MLCTy,\,T)},\,S_0} \approx 0$ and $S_{n(MLCTx,\,T)} \neq S_{n(MLCTy,\,T)}$ (this statement is described in S6A, pages S83−S87), then the fundamental expression for $\iota_{em(p)}$ in eq 8 based on eqs 3 and 5 can be given by[73]

$$\begin{aligned}\iota_{em(p)} &= \frac{k_{RAD(p)}}{(\nu_{T_e,S_0})^3} \\ &= \frac{C_R}{C_f}\left|\sum_X \sum_{S_{n(T)}}\left[\frac{H^{SOC}_{X(T_e,S_{n(T)})}}{\Delta E_{T_e,S_{n(T)}}}\sqrt{\frac{f_{S_{n(T)},S_0}(X)}{\nu_{S_{n(T)},S_0}}}\right]\right|^2 \\ &\approx C_i \sum_X \sum_{S_{n(T)}}\left[\left(\frac{H^{SOC}_{X(T_e,S_{n(T)})}}{\Delta E_{T_e,S_{n(T)}}}\right)^2 \times \frac{f_{S_{n(T)},S_0}(X)}{\nu_{S_{n(T)},S_0}}\right] \\ &\approx C_i \sum_X \sum_{S_{n(T)}}[(H^{SOC}_{X(T_e,S_{n(T)})})^2 \times f_{EW(S_{n(T)})}(X)]\end{aligned} \quad (8)$$

where $f_{EW(S_{n(T)})} = \frac{f_{S_{n(T)},S_0}}{(\Delta E_{T_e,S_{n(T)}})^2 \times \nu_{S_{n(T)},S_0}}$, $C_i = C_R/C_f$ (the definition of C_f is shown in eq S4g, page S54), $\Delta E_{T_e - S_{n(T)}} \approx E_{S_{n(T)}} + \lambda_{reg(T)} - h\nu_{em(\,max\,)}$ (see the term definition of $\Delta E_{T_e - S_{n(T)}}$ in Figure S5A, page S68), and X is the D^{SOC}-type (X = D) or A^{SOC}-type (X = A) mediation operation. The simple $\iota_{em(p)}$ equation focuses on the D^{SOC} mechanism shown in eqs S4g−S4l, pages S54−S55.

The f_{EW} term in eq 8 is called the energy-weighted oscillator strength.[73] Additionally, if $H^{SOC}_{X(T_e,\,S_{n(T)})}$ in eq 8 is assumed to be constant for the SOC-efficient $S_{n(T)}$ excited states of types D^{SOC} and A^{SOC} (this statement for the D^{SOC}-type configuration is described in the S6B section, page S87), then, $\iota_{em(p)}$ can be represented as

$$\iota_{em(p)} \approx C_i \sum_X \left[(H^{SOC}_{X(T_e,S_{n(T)})})^2 \sum_{S_{n(T)}} f_{EW(S_{n(T)})}(X)\right] \quad (9)$$

Configurations of Natural Transition Orbitals (NTOs) and Parameters of ∑SOCM-IS for the Low-Energy Singlet Excited State in the T_e Coordinates of the Complexes. Fundamentally, the $\iota_{em(p)}$ amplitude is dependent on the efficiency of the vertical SOC configurations between the T_e and the intense low-energy S_n states in the T_e geometry ($S_{n(T)}$), and subsequent NTO analyses are based on this logical notion. The plots of the NTOs for vertical $S_{n(T)}$ transitions (in the T_e geometry) of the $[Ru(bpy)(NH_3)_4]^{2+}$,[73] $[Ru(bpy)(en)_2]^{2+}$,[107] $[Ru(bpy)_2(en)]^{2+}$,[73,107] and $[Ru(bpy)_2(ppy)]^{+}$[73] complexes were reported in the previous studies, and the orbital compositions of the NTOs of the T_e and low-energy $S_{n(T)}$ states of $[Ru(bpy)_2(en)]^{2+}$, $[Ru(bpy)(en)_2]^{2+}$, and $[Ru(bpy)(NH_3)_4]^{2+}$ are shown in Table S5C (page S75).

The illustrated NTOs of the low-energy $S_{n(T)}$ state for the $[Ru(bpy)_2(CM)]^+$ complexes are plotted in Figures 10 (CM = ppm) and 11 (CM = piQ). The orbital configurations in the donor and acceptor NTOs of the T_e and low-energy $S_{n(T)}$ states of the $[Ru(bpy)(NH_3)_4]^{2+}$,[73] $[Ru(bpy)(en)_2]^{2+}$,[107] $[Ru(bpy)_2(en)]^{2+}$,[73] and $[Ru(bpy)_2(CM)]^+$ complexes (CM = ppy[73] and ppm) show a simple n-, D^{SOC}-, and A^{SOC}-type SOC mediation. The postulated SOC-mediated relationships between the T_e and low-energy $S_{n(T)}$ states for $[Ru(bpy)_2(piQ)]^+$ and $[Ru(bpy)_2(dpz)]^+$ complexes show simple n, D^{SOC}, and A^{SOC} characteristics and significant $(A + D)^{SOC}$ characteristics ($S_{4(T)}$ and $S_{5(T)}$), as shown by the low-energy NTOs of $S_{n(T)}$ for $[Ru(bpy)_2(piQ)]^+$ in Figure 11. Information concerning the SOC-mediated relation of the T_e and low-energy $S_{n(T)}$ states for the target $[Ru(bpy)_2(CM)]^+$ complexes is provided in Table 2, and details of the NTO configurations are provided in Table S5B (page S71).

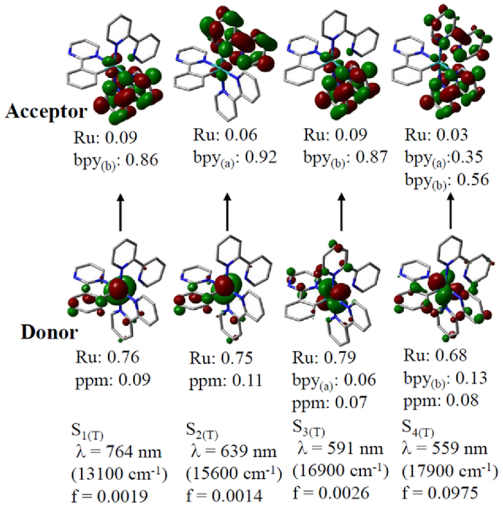

Figure 10. TDDFT-calculated NTOs of low-energy singlet excited states at the T_e coordinates ($S_{n(T)}$) of the $[Ru(bpy)_2(ppm)]^+$ ion; the moiety labels for the Δ-form target complexes are shown in Figure 8. The parameters in the panel include the Mulliken orbital population of moieties of the donor and acceptor NTOs, the calculated vertical transition energy (λ for wavelength, nm, with its energy conversion, cm^{-1}, in parentheses), and the oscillator strength of the target $S_{n(T)}$ states shown at the bottom (the definition of vertical transition energy is provided in Figure S5A, page S68).

Component of $\sum f_{EW(S_{n(T)})}$ of ∑SOCM-IS Modeling in Equation 9 Focusing on the Type D^{SOC}-Driven Contribution. Once again, the $\iota_{em(p)}$ amplitudes of the complexes are based on the 77 K observations and Einstein's formalism (eq 1). If we assume that the SOC efficiency of the complexes in this work is dominated by the donor SOMO-mediated (type D^{SOC}) configurational mixing between the $S_{n(T)}$ and T_e states, the postulation is that $H^{SOC}_{T_e,\,S_{n(T)}} \approx H^{SOC}_{D(T_e,\,S_{n(T)})} \gg H^{SOC}_{A(T_e,\,S_{n(T)})}$ in eq 9 and the $\iota_{em(p)}$ values are related only to the component of ∑SOCM-IS, the sum of the D^{SOC}-type energy-weighted oscillator strengths ($\sum f_{EW(S_{n(T)})}(D^{SOC})$), in eq 9. The plot of $\iota_{em(p)}$ vs $\sum f_{EW(S_{n(T)})}(D^{SOC})$ of the complexes (complexes 2, 4, 5, a, and d) in Figure 12 shows good linear relationships, but those of the $[Ru(bpy)_2(\pi_{Ar}\text{-CM})]^+$ ions, where π_{Ar}-CM = piQ (c) and dpz (e), are higher than the least-squares line that corresponds to 50% of the given $\sum f_{EW(S_{n(T)})}(D^{SOC})$ values,

https://doi.org/10.1021/acsomega.2c07276
ACS Omega 2022, 7, 48583−48599

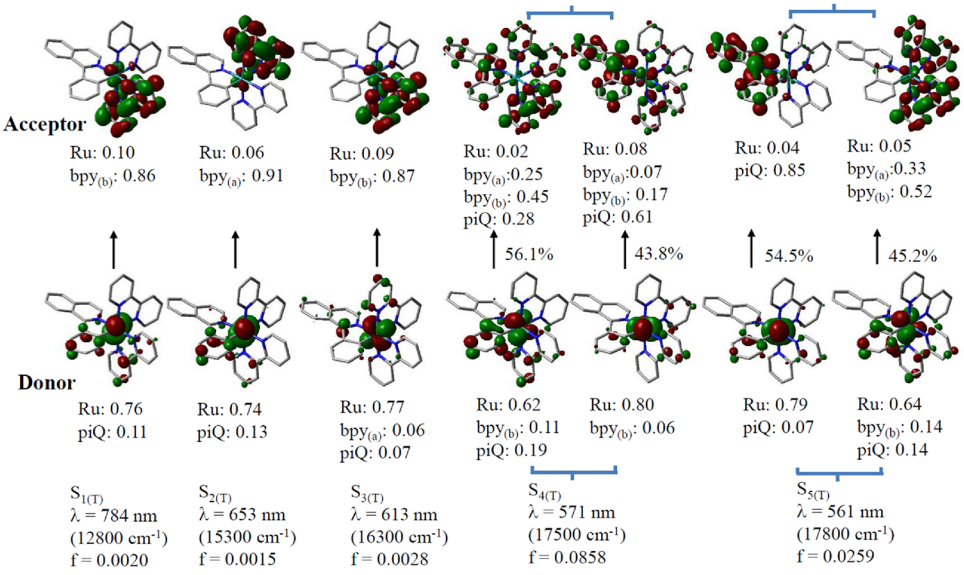

Figure 11. TDDFT-calculated NTOs of the low-energy singlet excited states (at T_e coordinates, $S_{n(T)}$) of the $[Ru(bpy)_2(piQ)]^+$ ion; the moiety labels for the Δ-form target complexes are shown in Figure 8. The parameters in the panel include the Mulliken orbital population of moieties of the donor and acceptor NTOs, the calculated vertical transition energy (λ for wavelength, nm, with its energy conversion, cm^{-1}, in parentheses), and the oscillator strength of the target $S_{n(T)}$ states shown at the bottom (the definition of vertical transition energy is provided in Figure S5A, page S68).

which is similar to the result for the plot of $\iota_{em(p)}$ versus $\int$SOCEWA $d\nu$ of the complexes in Figure 9. This phenomenon for the reference ($[Ru(bpy)_{3-n}(Am)_{2n}]^{2+}$, 2, 4, and 5) and the $[Ru(bpy)_2(sc\text{-}CM)]^+$ (sc-CM = ppy (a) and ppm (d)) complexes in Figure 12 is attributed to the primary-type D^{SOC}-mediated configurational mixing between the $S_{n(T)}$ and T_e states dominating the ∑SOCM-IS contributions to the $\iota_{em(p)}$ values, but this simple conclusion does not effectively explain the significantly high $\iota_{em(p)}$ values for the $[Ru(bpy)_2(\pi_{Ar}\text{-}CM)]^+$ reported in this work. In summary, the simple ∑SOCM-IS modeling focused on a limited-type D^{SOC}-mediated contribution does not effectively explain the observation of the remarkably high $\iota_{em(p)}$ amplitudes for the $[Ru(bpy)_2(\pi_{Ar}\text{-}CM)]^+$ complexes in Figure 12.

Presupposed $\sum f_{EW(S_{n(T)})}$ Amplitudes in Equation 9 Including the Overestimated Type A^{SOC}-Mediated Contribution. To verify the DFT results, the NTO plots of the low-energy $S_{n(T)}$ state for $[Ru(bpy)_{3-n}(Am)_{2n}]^{2+}$,[8,65,73,106,107] $[Ru(bpy)_2(sc\text{-}CM)]^+$ (sc-CM = ppy[73] and ppm), and $[Ru(bpy)_2(\pi_{Ar}\text{-}CM)]^+$ (π_{Ar}-CM = piQ and dpz) show that their acceptor SOMOs include significant dπ-Ru orbital components (2−10%, Ru is assumed to be a heavy atom), and the $\hat{H}^{SO}$construction in eqs 2 and 7 contains angular terms from all atoms, which suggests that the ∑SOCM-IS modeling for $\iota_{em(p)}$ related to the $\sum f_{EW(S_{n(T)})}$ amplitude should possibly consider the $\sum f_{EW(S_{n(T)})}$ containing both D^{SOC}- and A^{SOC}-type mediation contributions. The $\sum f_{EW(S_{n(T)})}(X)$ values of D^{SOC}- and A^{SOC}-type mediation (X = D and A) in eq 9 for the target complexes are shown in Figure S5D (page S77). The $f_{EW(S_{n(T)})}(X)$ amplitude for $(A + D)^{SOC}$-type $S_{n(T)}$ is considered to contribute to both the D^{SOC}- and A^{SOC}-type mediations, and the $\sum f_{EW(S_{n(T)})}(X)$ values of the low-energy $S_{n(T)}$ states of the complexes in Figure S5D (page S77) are shown in Table 2 and Table S5B,C (pages S71−S77). The $\sum f_{EW(S_{n(T)})}(A)/\sum f_{EW(S_{n(T)})}(D)$ ratios are approximately 0.2−0.3 for the $[Ru(bpy)_{3-n}(Am)_{2n}]^{2+}$ and $[Ru(bpy)_2(sc\text{-}CM)]^+$ complexes and 1.2−1.3 for $[Ru(bpy)_2(\pi_{Ar}\text{-}CM)]^+$ ions. To simply understand the logical relations of $\iota_{em(p)}$ versus the $\sum f_{EW(S_{n(T)})}(X)$ for ∑SOCM-IS modeling in eq 9 for the target complexes in this work and to presuppose $\sum f_{EW(S_{n(T)})}(X)$ amplitudes including the D^{SOC} and A^{SOC} components, two assumptions must be considered:

(1) We postulate that the $H^{SOC}_{D(T_e, S_{n(T)})}$ and $H^{SOC}_{A(T_e, S_{n(T)})}$ values are constants for the D^{SOC}- and A^{SOC}-type mediation relations in eq 9, respectively.

(2) If $H^{SOC}_{A(T_e, S_{n(T)})} = H^{SOC}_{D(T_e, S_{n(T)})}/4$, then the $H^{SOC}_{A(T_e, S_{n(T)})}$ value will be overestimated because most of the orbital population in the acceptor SOMOs is localized on the light atoms of the ligand moiety for the type A^{SOC} mediation relation in eq 7. As a result, the calculated $\sum f_{EW(S_{n(T)})}$ value from the D^{SOC}- and A^{SOC}-type mediation in eq 9 can be estimated.

Based on the two postulations above, eq 9 can be simplified to

$$\iota_{em(p)} \approx C_i(H^{SOC}_{D(T_e,S_{n(T)})})^2 \sum_{S_{n(T)}} f_{EW(S_{n(T)})} \quad (10)$$

where $\sum f_{EW(S_{n(T)})} = \sum f_{EW(S_{n(T)})}(D) + [\sum f_{EW(S_{n(T)})}(A)]/16$.

In the plot of $\iota_{em(p)}$ versus $\sum f_{EW(S_{n(T)})}$ based on eq 10 for the target complexes shown in Figure 13, the observed $\iota_{em(p)}$ amplitudes for $[Ru(bpy)_2(\pi_{Ar}\text{-}CM)]^+$ (π_{Ar}-CM = piQ (c) and dpz (d)) are above those of the least-squares line for the reference $[Ru(bpy)_{3-n}(Am)_{2n}]^{2+}$ (2, 4, and 5) and $[Ru(bpy)_2(sc\text{-}CM)]^+$ (a and d) complexes by approximately 30%, and even the $\sum f_{EW(S_{n(T)})} = \sum f_{EW(S_{n(T)})}(D) + [\sum f_{EW(S_{n(T)})}(A)]/16$ amplitude overestimates the type A^{SOC}-mediated $\sum f_{EW(S_{n(T)})}(A)$ contribution in eq 10. These results suggest that the intensity term in the ∑SOCM-IS model that contains only D^{SOC}- and A^{SOC}-type contributions cannot effectively explain the remarkably high $\iota_{em(p)}$ amplitude of the Ru-bpy

https://doi.org/10.1021/acsomega.2c07276
ACS Omega 2022, 7, 48583−48599

Table 2. Characteristics of the SOC Mediation Types of Low-Energy Singlet Excited States in the T_e Geometry ($S_{n(T)}$) of Target $[Ru(bpy)_2(CM)]^+$ Ions[a]

excited state	L	SOC mediation type[b]	oscillator strength, f	excited-state energy, $cm^{-1}/10^3$	$f_{EW} \times 10^{13}$[c]
$S_{1(T)}$	ppy	type n	0.0018	12.64	
	ppm	type n	0.0019	13.09	
	piQ	type n	0.0020	12.76	
	dpz	type n	0.0033	13.33	
$S_{2(T)}$	ppy	type A^{SOC}	0.0015	15.20	0.090
	ppm	type A^{SOC}	0.0014	15.65	0.077
	piQ	type A^{SOC}	0.0015	15.32	0.089
	dpz	type A^{SOC}	0.0016	15.87	0.082
$S_{3(T)}$	ppy	type D^{SOC}	0.0021	16.37	0.064
	ppm	type D^{SOC}	0.0026	16.92	0.070
	piQ	type D^{SOC}	0.0028	16.31	0.092
	dpz	type D^{SOC}	0.0026	17.39	0.059
$S_{4(T)}$	ppy	type D^{SOC}	0.0895	17.57	1.57
	ppm	type D^{SOC}	0.0975	17.89	1.713
	piQ	type $(A + D)^{SOC}$	0.0858	17.51	1.615
	dpz	type $(A + D)^{SOC}$	0.0881	17.95	1.575
$S_{5(T)}$	ppy	type n	0.0411	18.62	
	ppm	type n	0.0356	19.05	
	piQ	type $(A + D)^{SOC}$	0.0259	17.83	0.427
	dpz	type $(A + D)^{SOC}$	0.0191	18.18	0.310
$S_{6(T)}$	ppy	type n	0.0784	20.83	
	ppm	type A^{SOC}	0.0014	19.88	0.012
	piQ	type n	0.0370	18.76	
	dpz	type n	0.0355	19.34	
$S_{7(T)}$	ppy	type A^{SOC}	0.0038	21.10	0.021
	ppm	type n	0.0823	21.19	
	piQ	type n	0.1097	20.58	
	dpz	type n	0.0052	19.34	

[a]NTO configurations based on the DFT modeling are shown in Table S5B (page S71). [b]Definition of SOC-driven types describe in the first subsection of Discussion. [c]Equation 8.

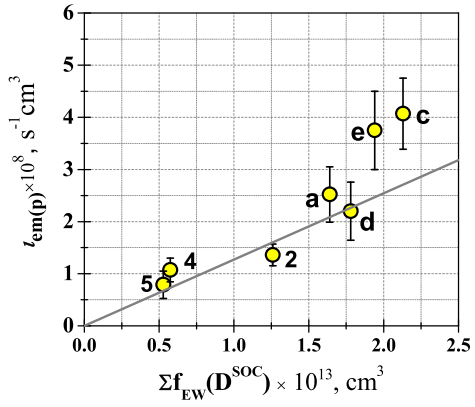

Figure 12. Illustration of the postulated dependencies of $\iota_{em(p)}$, $k_{RAD(p)}/(\nu_{ave})^3$, versus $\sum f_{EW(S_{n(T)})}(D^{SOC})$ (based on eq 9, if $H^{SOC}_{T_e, S_{n(T)}} \approx H^{SOC}_{D(T_e, S_{n(T)})} \gg H^{SOC}_{A(T_e, S_{n(T)})}$) for several Ru-bpy chromophores: $[Ru(bpy)_2(CM)]^+$, (a, c−e codes in Figure 1); $[Ru(bpy)_2(en)]^{2+}$, 2; $[Ru(bpy)(en)_2]^{2+}$, 4; $[Ru(bpy)(NH_3)_4]^{2+}$, 5. The least-squares line including the target complexes (2, 4, and 5 and $[Ru(bpy)_2(sc\text{-}CM)]^+$ complexes; a and d) shows $R^2 = 0.92$ and slope = $(1.27 \pm 0.13) \times 10^5$.

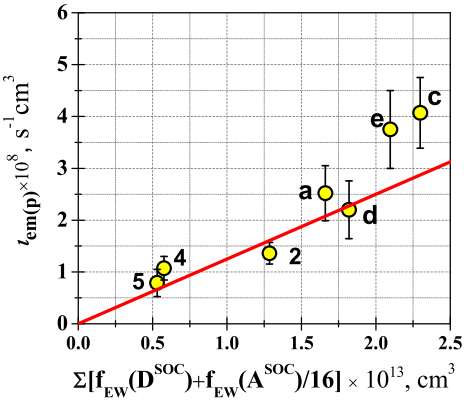

Figure 13. Illustration of the sum of the energy-weighted oscillator strengths of D^{SOC}- and A^{SOC}-type mediation, $\sum f_{EW(S_{n(T)})}(D) + [\sum f_{EW(S_{n(T)})}(A)]/16$, dependencies of $\iota_{em(p)}$ ($k_{RAD(p)}/(\nu_{ave})^3$) based on eq 10 for several Ru-bpy chromophores: $[Ru(bpy)_2(CM)]^+$, (a, c−e codes in Figure 1); $[Ru(bpy)_2(en)]^{2+}$, 2; $[Ru(bpy)(en)_2]^{2+}$, 4; $[Ru(bpy)(NH_3)_4]^{2+}$, 5. The least-squares line is based on the parameters of the target complexes (2, 4, 5, and $[Ru(bpy)_2(sc\text{-}CM)]^+$ complexes; a and d), $R^2 = 0.95$ and slope = $(1.25 \pm 0.13) \times 10^5$.

chromophore of $[Ru(bpy)_2(\pi_{Ar}\text{-}CM)]^+$ ions compared to those of the reference and $[Ru(bpy)_2(sc\text{-}CM)]^+$ complexes. A possible solution to this issue is to reconsider the perturbation principle of molecular orbitals and SOC fundamentals. The NTO plots of the low-energy $S_{n(T)}$ states for the $[Ru(bpy)_2(CM)]^+$ ions (see Figures 9 and 10) and $[Ru(bpy)(NH_3)_4]^{2+}$,[8,65,73,106] $[Ru(bpy)(en)_2]^{2+}$,[107] and $[Ru(bpy)_2(en)]^{2+}$[73,107] complexes show a significant contribution from the π-ligand component in the donor SOMOs related to the configurations between MLCT and $\pi\pi^*$-ligand states, suggesting that the efficient $\sum f_{EW(S_{n(T)})}$ in eq 9 should include the influence of the perturbation of the configuration of low-energy ^{1}MLCT and high-energy $^1\pi\pi$ states.

Intensity Perturbation of Configurational Mixing between Singlet Low-Energy MLCT and High-Energy $\pi\pi^*$-L_{Ar} Excited States in the $\sum$SOCM-IS Formalism. The unusually high $\iota_{em(p)}$ amplitudes observed for the $[Ru(bpy)_2(\pi_{Ar}\text{-}CM)]^+$ ions (c and e) in Figure 13 (based on eq 10) imply that the influence of the calculated $\sum f_{EW(S_{n(T)})}$ value for the efficient low-energy ^{1}MLCT excited states of D^{SOC}- and A^{SOC}-type contributions should not contain all of the significant intensity contributions from the singlet excited states in the $\sum$SOCM-IS modeling. Straightforward SOC mixing between T_e and high-energy singlet $\pi\pi^*$-L_{Ar} states ($^1\pi\pi^*$-L_{Ar}, L_{Ar} = aromatic ligand) is not taken into consideration in this work because only light atoms (C, H, and N) are present in the $^1\pi\pi^*$-L_{Ar} of the L_{Ar} moiety; this statement is described in the S6D section (page S89). In more detail, the configurational mixing between low-energy ^{1}MLCT (S_n) and high-energy $^1\pi\pi^*$-L_{Ar} (S_m) states should perturb the $\vec{M}_{S_{n(T)}, S_0}$ values in the $\iota_{em(p)}$ formalism, where the selected ^{1}MLCT ($S_{n(T)}$) should focus on D^{SOC}-type mediation ($H^{SOC}_{D(T_e, S_{n(T)})} \gg H^{SOC}_{A(T_e, S_{n(T)})}$ in eq 7) and $m > n$. The $\vec{M}_{S_{n(T)}, S_0}$ term in the $\iota_{em(p)}$ equation (eq 3) should include a linear combination of the $S_{n(T)}$ and $S_{m(T)}$ mixing perturbation, $\vec{M}_{S_{n(T)}, S_0} \approx \vec{M}^o_{S_{n(T)}, S_0} + \alpha_{S_{m(T)}, S_{n(T)}} \vec{M}^o_{S_{m(T)}, S_0} |\cos \theta_{m,n}|$, and the superscript "o" indicates the diabatic transition moment without $S_{n(T)}$ and $S_{m(T)}$ mixing, which can be treated in eq

https://doi.org/10.1021/acsomega.2c07276
ACS Omega 2022, 7, 48583−48599

11, where $\alpha_{S_{m(T)}, S_{n(T)}}$ is a mixing coefficient between $S_{n(T)}$ and $S_{m(T)}$. A detailed description of eq 11 is provided in Section S4C (page S59).

$$\iota_{em(p)} \equiv \frac{k_{RAD(p)}}{(\nu_{T_e,S_0})^3} = C_R \times \sum_{S_{n(T)}} \{(\alpha^{SOC}_{T_e,S_{n(T)}})^2 (\vec{M}_{S_{n(T)},S_0})^2\}$$
$$\approx C_i \times (H^{SOC}_{D(T_e,S_{n(T)})})^2 \left[\sum_{S_{n(T)}} f_{EW(S_{n(T)})}(D) + \sum (2^{nd}\text{-}f_{EW}) \right] \quad (11)$$

where the term,

$$\sum (2^{nd}\text{-}f_{EW}) = 2 \sum_{S_{n(T)}} \left[\left(\frac{1}{\Delta E_{T_e,S_{n(T)}}} \right)^2 \times \sum_{S_m} \left(\frac{H_{S_{m(T)},S_{n(T)}}}{\Delta E_{S_{m(T)},S_{n(T)}}} \sqrt{\frac{f_{S_{n(T)},S_0}(D)}{\nu_{S_{n(T)}}}} \sqrt{\frac{f_{S_{m(T)},S_0}}{\nu_{S_{m(T)}}}} |\cos\theta_{m,n}| \right) \right]$$

in eq 11 is referred to as the sum of the second-order energy-weighted oscillator strength, $\sum(2^{nd} - f_{EW})$, from the intensity perturbation of the configuration of low-energy ^{1}MLCT ($S_{n(T)}$) and high-energy $^1\pi\pi^*$-L_{Ar} ($S_{m(T)}$) excited states, and the $\Delta E_{S_{m(T)}, S_{n(T)}}$ is the energy difference between the $S_{m(T)}$ and $S_{n(T)}$ states (i.e., $E_{S_{m(T)}} - E_{S_{n(T)}} \approx \nu_{S_{n(T)}} - \nu_{S_{m(T)}}$). The formula derivation (eq 11) and its detailed description can be found in the S4C section (pages S59−S61).

If $|\cos\theta_{m,n}|$ in eq 11 is a constant for each pair of $S_{n(T)}/S_{m(T)}$ mixing perturbations, then this act is only for simplicity in the calculation; the calculated $\sum(2^{nd} - f_{EW})/|\cos\theta_{m,n}|$ values of the target complexes in a weak coupling setting ($H_{S_{m(T)}, S_{n(T)}}$ = 1000 cm^{-1} and $\Delta E_{S_{m(T)}, S_{n(T)}}$ > 10,000 cm^{-1}, $\alpha_{S_{m(T)}, S_{n(T)}}$ < 0.1) are shown in Tables S5C1−S5C5 (pages S78−S82). Furthermore, the calculated $\sum(2^{nd} - f_{EW})/|\cos\theta_{m,n}|$ values of the target complexes in Tables S5C1−S5C5 with intense low-energy $S_{n(T)}$ (D^{SOC}-mediated ^{1}MLCT) and intense high-energy $S_{m(T)}$ (inter- and intra-$^1\pi\pi^*$-L_{Ar}, $f_{S_{m(T)}, S_0}$ > 0.03) states are based on the parameters of DFT modeling. The estimated $\sum(2^{nd} - f_{EW})/|\cos\theta_{m,n}|$ values of the $[Ru(bpy)_2(sc\text{-}CM)]^+$ ions (sc-CM = ppy and ppm) are approximately 1.7 times higher than the corresponding values of the $[Ru(bpy)_2(en)]^{2+}$, and the $\sum(2^{nd} - f_{EW})/|\cos\theta_{m,n}|$ values of the $[Ru(bpy)_2(\pi_{Ar}\text{-}CM)]^+$ ions (π_{Ar}-CM = dpz and piQ) are approximately 1.5-fold greater than those of the $[Ru(bpy)_2(sc\text{-}CM)]^+$ ions. The above results can be attributed to the following facts (see Tables S5S1C1−S5C5, pages S78−S82): (1) every $[Ru(bpy)_2(CM)]^+$ ion has 7−8 intense $S_{m(T)}$ excited states, and $[Ru(bpy)_2(en)]^{2+}$ has only 3 intense-$S_{m(T)}$ excited states ($f_{S_{m(T)}, S_0}$> 0.03); (2) the $[Ru(bpy)_2(\pi_{Ar}\text{-}CM)]^+$ ions (c and e) have relatively lower-energy intense-$S_{m(T)}$ excited states ($\nu_{S_{m(T)}}$ in 31,000−35,340 cm^{-1}) compared to those of $[Ru(bpy)_2(sc\text{-}CM)]^+$ (a, b, and d; $\nu_{S_{m(T)}}$ in 34,000−37,340 cm^{-1}), and $\nu_{S_{m(T)}}$ is related to the terms of $\frac{1}{\Delta E_{S_{m(T)},S_{n(T)}}} \times \sqrt{\frac{1}{\nu_{S_{m(T)}}}}$ in $\sum(2^{nd} - f_{EW})$ of eq 11; (3) each of $[Ru(bpy)_2(en)]^{2+}$ and $[Ru(bpy)_2(sc\text{-}CM)]^+$ ions has only an intense low-energy D^{SOC}-type ^{1}MLCT excited state, but each $[Ru(bpy)_2(\pi_{Ar}\text{-}CM)]^+$ ion has two intense low-energy (A + D)^{SOC}-type ^{1}MLCT excited states; (4) concerning the above products, the values for the sum of second-order components in $\sum(2^{nd} - f_{EW})/|\cos\theta_{m,n}|$ for $[Ru(bpy)_2(\pi_{Ar}\text{-}CM)]^+$ ions are greater than that for the corresponding values of $[Ru(bpy)_2(sc\text{-}CM)]^+$ ions, and the $\sum(2^{nd} - f_{EW})/|\cos\theta_{m,n}|$ values for the $[Ru(bpy)_2(sc\text{-}CM)]^+$ ions are greater than those of $[Ru(bpy)_2(en)]^{2+}$; (5) the point (2) above should be regarded as the relatively low-energy intense-$S_{m(T)}$ configurations including a significant $\pi\pi^*$-CM component for $[Ru(bpy)_2(\pi_{Ar}\text{-}CM)]^+$, but the first two low-energy intense-$S_{m(T)}$ configurations only include the $\pi\pi^*$-bpy component for $[Ru(bpy)_2(sc\text{-}CM)]^+$. This consequence of the unusually high $\iota_{em(p)}$ value of the $[Ru(bpy)_2(\pi_{Ar}\text{-}CM)]^+$ ion in Figure 12 can be attributed to both significantly high $\sum f_{EW(S_{n(T)})}$ and $\sum(2^{nd} - f_{EW})$ contributions in the $\sum$SOCM-IS formalism. However, due to the uncertain $|\cos\theta_{m,n}|$ magnitude between the efficient low-energy ^{1}MLCT (S_n) and high-energy $^1\pi\pi^*$-L_{Ar} (S_m) transition states, the only plausible $\sum(2^{nd} - f_{EW})/|\cos\theta_{m,n}|$ components can be displayed, and the $\sum(2^{nd} - f_{EW})$ value cannot be evaluated in this work.

In summary, recent reports have included the use of computational SOCM-IS modeling to fit the observed singlet-to-triplet absorption and phosphorescence parameters of target M-L_{Ar}-type complexes, and their modeling is attributed to the primary ΣSOCM-IS contribution from the intense low-energy $S_{n(T)}$ states.[66,124−130] In this work, the observed $\iota_{em(p)}$ magnitudes of the $[Ru(bpy)_2(\pi_{Ar}\text{-}CM)]^+$ ions were found to be considerably higher than those of the $[Ru(bpy)_2(sc\text{-}CM)]^+$ and $[Ru(bpy)_{3-n}(Am)_{2n}]^{2+}$ complexes at the given $\int$SOCEWA $d\nu$ (Figure 9, based on eq 6) and at the given $\sum f_{EW(S_{n(T)})}(D)$ values (Figure 12, based on eq 9), suggesting that the $\iota_{em(p)}$ formalism based on the simple $\sum f_{EW(S_{n(T)})}$ formalism from low-energy ^{1}MLCT states should not contain all of the significant intensity contributions in the $\sum$SOCM-IS model. In this work, we consider the $\sum(2^{nd} - f_{EW})$ value obtained from intensity perturbation of the configurations between low-energy ^{1}MLCT and high-energy $^1\pi\pi$-(L_{Ar}) states, which significantly contributes to the $\iota_{em(p)}$ magnitude in the $\sum$SOCM-IS formalism (eq 11) for the Ru-bpy phosphorescence chromophore of the $[Ru(bpy)_2(CM)]^+$ complex system.

CONCLUSIONS

This study represents a continuation of our work directed toward understanding the meaning of the intrinsic phosphorescence efficiency, $\iota_{em(p)} = k_{RAD(p)}/(\nu_{ave})^3$, of Ru-bpy phosphorescence chromophores for $[Ru(bpy)_2(CM)]^+$ and the reference $[Ru(bpy)_{3-n}(Am)_{2n}]^{2+}$ series. The phenomenon of variation in $\iota_{em(p)}$ for complex series is considered to be related to spin−orbit coupling (SOC)-mediated intensity stealing (SOCM-IS) from efficient singlet states, which is based on low-temperature observations, DFT modeling, and basic SOC principles.[73] The parameters for the orbital comparison for transition states in DFT modeling helped in the analysis of data concerning the SOCM-IS construct.

The plot in Figure 6 shows that the observed $\iota_{em(p)}$ magnitudes of the Ru-bpy chromophore for the $[Ru(bpy)_2(CM)]^+$ ions in the given emission energy region are

https://doi.org/10.1021/acsomega.2c07276
ACS Omega 2022, 7, 48583−48599

clearly higher than the corresponding values for $[Ru(bpy)_{3-n}(Am)_{2n}]^{2+}$ ions. The $\iota_{em(p)}$ values of the $[Ru(bpy)_2(\pi_{Ar}\text{-CM})]^+$ ions (π_{Ar}-CM = dpz and piQ; π-rich cyclometalated ligand) were approximately twofold higher than those of the $[Ru(bpy)_2(sc\text{-CM})]^+$ complexes (sc-CM = ppy, bhq, and ppm; a simply constructed cyclometalated ligand).

The observed $\iota_{em(p)}$ variation of the $[Ru(bpy)_{3-n}(Am)_{2n}]^{2+}$ and $[Ru(bpy)_2(sc\text{-CM})]^+$ complexes can be attributed to the change in the sum of the energy-weighted oscillator strengths from the low-energy $S_n(^1MLCT)$ states of a type D^{SOC} mediation ($\sum f_{EW(S_{n(T)})}(D)$, see Figure 12), based on eqs 8 and 9 of the ∑SOCM-IS expression, but the unusually high $\iota_{em(p)}$ magnitudes of the $[Ru(bpy)_2(\pi_{Ar}\text{-CM})]^+$ ions in the given $\sum f_{EW(S_{n(T)})}(D)$ magnitude cannot account for this simple conclusion. However, the significantly high $\iota_{em(p)}$ values for the $[Ru(bpy)_2(\pi_{Ar}\text{-CM})]^+$ ions are not a simple result of the $\sum f_{EW(S_{n(T)})}$ contribution from the low-energy $S_n(^1MLCT)$ states of D^{SOC}- and A^{SOC}-type mediation (see Figures 12 and 13).

Again, the basic intensity factors for the ∑SOCM-IS expression in eqs 8 and 9 do not directly include the straightforward SOC configurations of the T_e and high-energy $^1\pi\pi^*\text{-}L_{Ar}$ states in this work (this statement is expressed in Section S6D, pages S89 and S90, and L_{Ar} is an aromatic-type ligand), but the second-order intensity perturbation ($\sum(2^{nd}\text{-}f_{EW})$) to the ∑SOCM-IS expression from the significant configurations of low-energy ^{1}MLCT(Ru-bpy) and high-energy $^1\pi\pi^*\text{-}L_{Ar}$ states should be considered. The values for the calculated $\sum(2^{nd}\text{-}f_{EW})$ component, $\sum(2^{nd}\text{-}f_{EW})/|\cos\theta_{m,n}|$, of the $[Ru(bpy)_2(\pi_{Ar}\text{-CM})]^+$ complexes were determined to be approximately 1.5-fold higher than the corresponding values for the $[Ru(bpy)_2(sc\text{-CM})]^+$ ions.

The current study, which contains experimental low-temperature observations, simple DFT modeling, and elementary parameters based on SOC principles, suggests that the remarkable high $\iota_{em(p)}$ magnitudes of the $[Ru(bpy)_2(\pi_{Ar}\text{-CM})]^+$ complexes can be attributed to both their $\sum f_{EW(S_{n(T)})}(D)$ and $\sum(2^{nd}\text{-}f_{EW})$ magnitudes in the case where the ΣSOCM-IS expression is greater than those of the $[Ru(bpy)_2(sc\text{-CM})]^+$ complexes.

■ ASSOCIATED CONTENT

Supporting Information

The Supporting Information is available free of charge at https://pubs.acs.org/doi/10.1021/acsomega.2c07276.

(S1) experimental section containing the materials and syntheses of the complexes, instrumentation, NMR spectra of the target complexes, and single-crystal X-ray data parameters of $[Ru(bpy)_2(dpz)](PF_6)\cdot(CH_2Cl_2)$; (S2) photophysical parameters for the reference $[Ru(bpy)_{3-n}(Am)_{2n}]^{2+}$ complexes and electrochemistry and low-temperature absorption spectra of the $[Ru(bpy)_2(CM)]^+$ ions; (S3) computational details and results of DFT modeling for the target $[Ru(bpy)_2(CM)]^+$ (CM = ppm, piQ, and dpz), including (1) DFT parameters for the compositions of HOMO-to-LUMO transitions in the low-energy S_n excited states, (2) comparison of the observed and DFT-calculated absorption curves of the target $[Ru(bpy)_2(CM)]^+$ ions, (3) DFT parameters of the S_n and T_n excited states, and (4) plots of the natural transition orbitals (NTOs) for the $S_{n(X)}$ and T_n excited states and (4) alpha (α) and beta (β) SOMOs of the $T_1(T_e)$ state for the target complexes; (S4) phosphorescence efficiency expression for the sum of the SOC-mediated intensity stealing (∑SOCM-IS) modeling and data analyses; (S5) parameters of the ∑SOCM-IS modeling based on SOC principles and primary DFT modeling; (S6) some conceptual details for the derivation process of the fundamental equation in Section S4 and manuscript (PDF)

■ AUTHOR INFORMATION

Corresponding Author

Yuan Jang Chen − *Department of Chemistry, Fu-Jen Catholic University, New Taipei City 24205, Taiwan, R.O.C.*; orcid.org/0000-0002-3134-8101; Phone: 886-2-2905-2490; Email: 054971@mail.fju.edu.tw

Authors

Yu Ru Chih − *Department of Chemistry, Fu-Jen Catholic University, New Taipei City 24205, Taiwan, R.O.C.*

Yu-Ting Lin − *Department of Chemistry, Fu-Jen Catholic University, New Taipei City 24205, Taiwan, R.O.C.*

Chi-Wei Yin − *Department of Chemistry, Fu-Jen Catholic University, New Taipei City 24205, Taiwan, R.O.C.*

Complete contact information is available at: https://pubs.acs.org/10.1021/acsomega.2c07276

Author Contributions

†Y.R.C., Y.-T.L., and C.-W.Y. contributed equally.

Funding

This work was funded (Y.J.C.) by the Ministry of Science and Technology (Taiwan, ROC) through grant MOST 109-2113-M-030-006.

Notes

The authors declare no competing financial interest.

■ ACKNOWLEDGMENTS

We wish to thank Prof. Hsing-Yin Chen (Department of Medicinal and Applied Chemistry, Kaohsiung Medical University) for help in building the DFT model (Gaussian 09) used in this work. We also wish to thank Prof. Ming-Kang Tsai (Department of Chemistry, National Taiwan Normal University) for help in building the ADF and DFT model (Gaussian 16) used in the S6E section of the SI. Authors thank Mr. Ting-Shen Kuo (Department of Chemistry, National Taiwan Normal University) for the parameters of the X-ray structure of $[Ru(bpy)_2(dpz)](PF_6)\cdot(CH_2Cl_2)$ in the S1B section in the SI.

■ REFERENCES

(1) Crosby, G. A.; Demas, J. N. Quantum Efficiencies of Transition-Metal Complexes. I. d-d Luminescence. *J. Am. Chem. Soc.* **1970**, *92*, 7262−7270.

(2) Demas, J. N.; Crosby, G. A. Quantum Efficiencies on Transition Metal Complexes. II. Charge-Transfer Luminescence. *J. Am. Chem. Soc.* **1971**, *93*, 2841−2847.

(3) Crosby, G. A. Spectroscopic Investigations of Excited States of Transition-Metal Complexes. *Acc. Chem. Res.* **1975**, *8*, 231−238.

(4) McCusker, J. K. Femtosecond Absorption Spectroscopy of Transition Metal Charge-Transfer Complexes. *Acc. Chem. Res.* **2003**, *36*, 876−887.

(5) Juris, A.; Balzani, V.; Barigelletti, F.; Campagna, S.; Belser, P.; von Zelewsky, A. Ru(II) Polypyridine Complexes: Photophysics, Photochemistry, Eletrochemistry, and Chemiluminescence. *Coord. Chem. Rev.* **1988**, *84*, 85−277.
(6) Sun, Q.; Mosquera-Vazquez, S.; Lawson Daku, L. M.; Guénée, L.; Goodwin, H. A.; Vauthey, E.; Hauser, A. Experimental Evidence of Ultrafast Quenching of the 3MLCT Luminescence in Ruthenium(II) Tris-bipyridyl Complexes Via a 3dd State. *J. Am. Chem. Soc.* **2013**, *135*, 13660−13663.
(7) Sun, Q.; Mosquera-Vazquez, S.; Suffren, Y.; Hankache, J.; Amstutz, N.; Lawson Daku, L. M.; Vauthey, E.; Hauser, A. On the Role of Ligand-Field States for the Photophysical Properties of Ruthenium(II) Polypyridyl Complexes. *Coord. Chem. Rev.* **2015**, *282-283*, 87−99.
(8) Lord, R. L.; Allard, M. M.; Thomas, R. A.; Odongo, O. S.; Schlegel, H. B.; Chen, Y.-J.; Endicott, J. F. Computational Modeling of the Triplet Metal-to-Ligand Charge-Transfer Excited-State Structures of Mono-Bipyridine−Ruthenium(II) Complexes and Comparisons to Their 77 K Emission Band Shapes. *Inorg. Chem.* **2013**, *52*, 1185−1198.
(9) Mazumder, S.; Thomas, R. A.; Lord, R. L.; Schlegel, H. B.; Endicott, J. F. A Density Functional Theory and Spectroscopic Study of Intramolecular Quenching of Metal-to-Ligand Charge-Transfer Excited States in Some Mono-Bipyridine Ruthenium(II) Complexes. *Can. J. Chem.* **2014**, *92*, 996−1009.
(10) McClure, D. S. Triplet-Singlet Transitions in Organic Molecules. Lifetime Measurements of the Triplet State. *J. Chem. Phys.* **1949**, *17*, 905−913.
(11) McClure, D. S. Spin-Orbit Interaction in Aromatic Molecules. *J. Chem. Phys.* **1952**, *20*, 682.
(12) Birks, J. B. *Photophysics of Aromatic Molecules*; Wiley-Interscience: New York, 1970.
(13) Bixon, M.; Jortner, J.; Verhoeven, J. W. Lifetimes for Radiative Charge Recombination in Donor-Acceptor Molecules. *J. Am. Chem. Soc.* **1994**, *116*, 7349−7355.
(14) Yersin, H.; Rausch, A. F.; Czerwieniec, R.; Hofbeck, T.; Fischer, T. The Triplet State of Organo-transition Metal Compounds. Triplet Harvesting and Singlet Harvesting for Efficient OLEDs. *Coord. Chem. Rev.* **2011**, *255*, 2622−2652.
(15) Powell, B. J. Theories of Phosphorescence in Organo-Transition Metal Complexes − From Relativistic Effects to Simple Models and Design Principles for Organic Light-Emitting Diodes. *Coord. Chem. Rev.* **2015**, *295*, 46−79.
(16) Bloino, J.; Biczysko, M.; Santoro, F.; Barone, V. General Approach to Compute Vibrationally Resolved One-Photon Electronic Spectra. *J. Chem. Theory Comput.* **2010**, *6*, 1256−1274.
(17) Concepcion, J. J.; Jurss, J. W.; Brennaman, M. K.; Hoertz, P. G.; Patrocinio, A. O. T.; Murakami Iha, N. Y.; Templeton, J. L.; Meyer, T. J. Making Oxygen with Ruthenium Complexes. *Acc. Chem. Res.* **2009**, *42*, 1954−1965.
(18) Meyer, T. J. Chemical Approaches to Artificial Photosynthesis. *Acc. Chem. Res.* **1989**, *22*, 163−170.
(19) Morris, A. J.; Meyer, G. J.; Fujita, E. Molecular Approaches to the Photocatalytic Reduction of Carbon Dioxide for Solar Fuels. *Acc. Chem. Res.* **2009**, *42*, 1983−1994.
(20) Alstrum-Acevedo, J. H.; Brennaman, M. K.; Meyer, T. J. Chemical Approaches to Artificial Photosynthesis. 2. *Inorg. Chem.* **2005**, *44*, 6802−6827.
(21) Chakraborty, S.; Wadas, T. J.; Hester, H.; Schmehl, R.; Eisenberg, R. Platinum Chromophore-Based Systems for Photo-induced Charge Separation: A Molecular Design Approach for Artificial Photosynthesis. *Inorg. Chem.* **2005**, *44*, 6865−6878.
(22) Grätzel, M. Solar Energy Conversion by Dye-Sensitized Photovoltaic Cells. *Inorg. Chem.* **2005**, *44*, 6841−6851.
(23) Magnuson, A.; Anderlund, M.; Johansson, O.; Lindblad, P.; Lomoth, R.; Polivka, T.; Ott, S.; Stensjö, K.; Styring, S.; Sundström, V.; et al. Biomimetic and Microbial Approaches to Solar Fuel Generation. *Acc. Chem. Res.* **2009**, *42*, 1899−1909.
(24) Meyer, G. J. Molecular Approaches to Solar Energy Conversion with Coordination Compounds Anchored to Semiconductor Surfaces. *Inorg. Chem.* **2005**, *44*, 6852−6864.
(25) Finkenzeller, W. J.; Hofbeck, T.; Thompson, M. E.; Yersin, H. Triplet State Properties of the OLED Emitter Ir(btp)2(acac): Characterization by Site-Selective Spectroscopy and Application of High Magnetic Fields. *Inorg. Chem.* **2007**, *46*, 5076−5083.
(26) Mills, I. N.; Porras, J. A.; Bernhard, S. Judicious Design of Cationic, Cyclometalated Ir(III) Complexes for Photochemical Energy Conversion and Optoelectronics. *Acc. Chem. Res.* **2018**, *51*, 352−364.
(27) Rausch, A. F.; Thompson, M. E.; Yersin, H. Matrix Effects on the Triplet State of the OLED Emitter Ir(4,6-dFppy)2(pic) (FIrpic): Investigations by High-Resolution Optical Spectroscopy. *Inorg. Chem.* **2009**, *48*, 1928−1937.
(28) Scholz, S.; Kondakov, D.; Lüssem, B.; Leo, K. Degradation Mechanisms and Reactions in Organic Light-Emitting Devices. *Chem. Phys.* **2015**, *115*, 8449−8503.
(29) Tsuboyama, A.; Iwawaki, H.; Furugori, M.; Mukaide, T.; Kamatani, J.; Igawa, S.; Moriyama, T.; Miura, S.; Takiguchi, T.; Okada, S.; et al. Homoleptic Cyclometalated Iridium Complexes with Highly Efficient Red Phosphorescence and Application to Organic Light-Emitting Diode. *J. Am. Chem. Soc.* **2003**, *125*, 12971−12979.
(30) Yam, V. W.-W.; Au, V. K.-M.; Leung, S. Y.-L. Light-Emitting Self-Assembled Materials Based on d8 and d10 Transition Metal Complexes. *Chem. Rev.* **2015**, *115*, 7589−7728.
(31) Yanai, N.; Kimizuka, N. New Triplet Sensitization Routes for Photon Upconversion: Thermally Activated Delayed Fluorescence Molecules, Inorganic Nanocrystals, and Singlet-to-Triplet Absorption. *Acc. Chem. Res.* **2017**, *50*, 2487−2495.
(32) Dobrucki, J. W. Interaction of Oxygen-Sensitive luminescent Probes Ru(phen)32+ and Ru(bipy)32+ with Animal and Plant Cells in Vitro: Mechanism of Phototoxicity and Conditions for Non-Invasive Oxygen Measurements. *J. Photochem. Photobiol., B* **2001**, *65*, 136−144.
(33) Dunphy, I.; Vinogradov, S. A.; Wilson, D. F. Oxyphor R2 and G2: Phosphors for Measuring Oxygen by Oxygen-Dependent Quenching of Phosphorescence. *Anal. Biochem.* **2002**, *310*, 191−198.
(34) Esipova, T. V.; Karagodov, A.; Miller, J.; Wilson, D. F.; Busch, T. M.; Vinogradov, S. A. Two New "Protected" Oxyphors for Biological Oximetry: Properties and Application in Tumor Imaging. *Anal. Chem.* **2011**, *83*, 8756−8765.
(35) Ji, J.; Rosenzweig, N.; Jones, I.; Rosenzweig, Z. Novel Fluorescent Oxygen Indicator for Intracellular Oxygen Measurements. *J. Biomed. Opt.* **2002**, *7*, 404−409.
(36) Komatsu, H.; Yoshihara, K.; Yamada, H.; Kimura, Y.; Son, A.; Nishimoto, S.-i.; Tanabe, K. Ruthenium Complexes with Hydrophobic Ligands That Are Key Factors for the Optical Imaging of Physiological Hypoxia. *Chem. − Eur. J.* **2013**, *19*, 1971−1977.
(37) Koren, K.; Dmitriev, R. I.; Borisov, S. M.; Papkovsky, D. B.; Klimant, I. Complexes of Ir^{III}-Octaethylporphyrin with Peptides as Probes for Sensing Cellular O_2. *ChemBioChem* **2012**, *13*, 1184−1190.
(38) Liu, J.-N.; Bu, W.; Shi, J. Chemical Design and Synthesis of Functionalized Probes for Imaging and Treating Tumor Hypoxia. *Chem. Rev.* **2017**, *117*, 6160−6224.
(39) Lowry, M. S.; Bernhard, S. Synthetically Tailored Excited States: Phosphorescent, Cyclometalated Iridium(III) Complexes and Their Applications. *Chem. − Eur. J.* **2006**, *12*, 7970−7977.
(40) Lucky, S. S.; Soo, K. C.; Zhang, Y. Nanoparticles in Photodynamic Therapy. *Chem. Rev.* **2015**, *115*, 1990−2042.
(41) Xie, Z.; Ma, L.; deKrafft, K. E.; Jin, A.; Lin, W. Porous Phosphorescent Coordination Polymers for Oxygen Sensing. *J. Am. Chem. Soc.* **2010**, *132*, 922−923.
(42) Zhang, S.; Hosaka, M.; Yoshihara, T.; Negishi, K.; Iida, Y.; Tobita, S.; Takeuchi, T. Phosphorescent Light−Emitting Iridium Complexes Serve as a Hypoxia-Sensing Probe for Tumor Imaging in Living Animals. *Cancer Res.* **2010**, *70*, 4490−4498.
(43) Balzani, V.; Ceroni, P.; Juris, A. *Photochemistry and Photophysics*; Wiley-VCH: Weinheim, Germany, 2014.

https://doi.org/10.1021/acsomega.2c07276
ACS Omega 2022, 7, 48583−48599

(44) Brunold, T. C.; Gudel, H. U. Luminescence Spectroscopy. In *Inorganic Electronic Structure and Spectroscopy*; Solomon, E. I.; Lever, A. B. P., Eds.; Wiley-Interscience: New York, 1999; pp. 259−306.
(45) Englman, R.; Jortner, J. The Energy Gap Law for Radiationless Transitions in Large Molecules. *Mol. Phys.* **1970**, *18*, 145−164.
(46) Gould, I. R.; Noukakis, D.; Gomez-Jahn, L.; Young, R. H.; Goodman, J. L.; Farid, S. Radiative and Nonradiative Electron Transfer in Contact Radical-ion Pairs. *Chem. Phys.* **1993**, *176*, 439−456.
(47) Henry, B. R.; Kasha, M. Radiationless Molecular Electronic Transitions. *Ann. Rev. Phys. Chem.* **1968**, *19*, 161−192.
(48) Kasha, M. Characterization of Electronic Transitions in Complex Molecules. *Discuss. Faraday Soc.* **1950**, *9*, 14−19.
(49) Speiser, S. Photophysics and Mechanisms of Intramolecular Electronic Energy Transfer in Bichromophoric Molecular Systems: Solution and Supersonic Jet Studies. *Chem. Rev.* **1996**, *96*, 1953−1976.
(50) Steinfeld, J. I. *Molecules and Radiation, an Introduction to Modern Molecular Spectroscopy*; MIT Press: Cambridge: MA, 1981.
(51) Jortner, J. Electronic Relaxation Processes in Large Molecules. *Pure Appl. Chem.* **1970**, *24*, 165−202.
(52) Jortner, J.; Rice, S. A.; Hochstrasser, R. Radiationless Transitions and Photochemistry. In *Advances in Photochemistry*; Pitts, B. O.; Hammond, J., Eds.; John Wiley Inc.: New York, 2007; p 149.
(53) Lin, S. H. Rate of Interconversion of Electronic and Vibrational Energy. *J. Chem. Phys.* **1966**, *44*, 3759−3767.
(54) Robinson, G. W.; Frosch, R. P. Theory of Electronic Energy Relaxation in the Solid Phase. *J. Chem. Phys.* **1962**, *37*, 1962−1973.
(55) Robinson, G. W.; Frosch, R. P. Electronic Excitation Transfer and Relaxation. *J. Chem. Phys.* **1963**, *38*, 1187−1203.
(56) Siebrand, W. Mechanism of Radiationless Triplet Decay in Aromatic Hydrocarbons and the Magnitude of the Franck—Condon Factors. *J. Chem. Phys.* **1966**, *44*, 4055−4057.
(57) Strickler, S. J.; Berg, R. A. Relationship between Absorption Intensity and Fluorescence Lifetime of Molecules. *J. Chem. Phys.* **1962**, *37*, 814−822.
(58) Mukherjee, T.; Ito, N.; Gould, I. R. Experimental Exploration of the Mulliken−Hush Relationship for Intramolecular Electron Transfer Reactions. *J. Phys. Chem. A* **2011**, *115*, 1837−1843.
(59) Mulliken, R. S.; Person, W. B. *Molecular Complexes*; Wiley-Interscience: New York, 1967.
(60) Hush, N. S. Intervalence-Transfer Absorption. Part 2. Theoretical Considerations and Spectroscopic Data. *Prog. Inorg. Chem.* **1967**, *8*, 391−444.
(61) Richardson, D. E.; Taube, H. Mixed-Valence Molecules: Electronic Delocalization and Stabilization. *Coord. Chem. Rev.* **1984**, *1984*, 107−129.
(62) Endicott, J. F. Modifications of Transition-Metal Reaction Patterns Through the Manipulation of Superexchange Couplings. *Acc. Chem. Res.* **1988**, *21*, 59−66.
(63) Newton, M. D. Quantum Chemical Probes of Electron-transfer Kinetics: the Nature of Donor-acceptor Interactions. *Chem. Rev.* **1991**, *91*, 767−792.
(64) Creutz, C.; Newton, M. D.; Sutin, N. Metal—Lingad and Metal—Metal Coupling Elements. *J. Photochem. Photobiol., A* **1994**, *82*, 47−59.
(65) Thomas, R. A.; Tsai, C. N.; Mazumder, S.; Lu, I. C.; Lord, R. L.; Schlegel, H. B.; Chen, Y. J.; Endicott, J. F. Energy Dependence of the Ruthenium(II)-Bipyridine Metal-to-Ligand-Charge-Transfer Excited State Radiative Lifetimes: Effects of $\pi\pi^*$(bipyridine) Mixing. *J. Phys. Chem. B* **2015**, *119*, 7393−7406.
(66) Heully, J.-L.; Alary, F.; Boggio-Pasqua, M. Spin-Orbit Effects on the Photophysical Properties of Ru(bpy)32+. *J. Chem. Phys.* **2009**, *131*, 184308.
(67) McGlynn, S. P.; Azumi, T.; Kinoshita, M. *Molecular Spectroscopy of the Triplet State*; Prentice-Hall: Englewood Cliffs, 1969.
(68) Condon, E. U.; Shortley, G. H. *The Theory of Atomic Spectra*; Cambridge University: Cambridge, UK, 1957.
(69) Koseki, S.; Gordon, M. S.; Schmidt, M. W.; Matsunaga, N. Main Group Effective Nuclear Charges for Spin-Orbit Calculations. *J. Phys. Chem.* **1995**, *99*, 12764−12772.
(70) Koseki, S.; Schmidt, M. W.; Gordon, M. S. Effective Nuclear Charges for the First- through Third-Row Transition Metal Elements in Spin−Orbit Calculations. *J. Phys. Chem. A* **1998**, *102*, 10430−10435.
(71) Marian, C. M. Understanding and Controlling Intersystem Crossing in Molecules. *Ann. Rev. Phys. Chem.* **2021**, *72*, 617−640.
(72) Obara, S.; Itabashi, M.; Okuda, F.; Tamaki, S.; Tanabe, Y.; Ishii, Y.; Nozaki, K.; Haga, M.-a. Highly Phosphorescent Iridium Complexes Containing Both Tridentate Bis(benzimidazolyl)-benzene or -pyridine and Bidentate Phenylpyridine: Synthesis, Photophysical Properties, and Theoretical Study of Ir-Bis(benzimidazolyl)benzene Complex. *Inorg. Chem.* **2006**, *45*, 8907−8921.
(73) Zhang, X. Z.; Cheng, C. C.; Chih, Y. R.; Lin, Y.-T.; Chen, H.-Y.; Chen, Y. J.; Endicott, J. F. Low Temperature Spectra and Density Functional Theory Modeling of Ru(II)-bipyridine Complexes with Cyclometalated Ancillary Ligands: The Excited State Spin-Orbit Coupling Origin of Variations in Emission Efficiencies. *J. Phys. Chem. A* **2019**, *123*, 9431−9449.
(74) Eng, J.; Gourlaouen, C.; Gindensperger, E.; Daniel, C. Spin-Vibronic Quantum Dynamics for Ultrafast Excited-State Processes. *Acc. Chem. Res.* **2015**, *48*, 809−817.
(75) Day, P.; Sanders, N. The Spectra of Complexes of Conjugated Ligands. Part II. Charge-Transfer in Substituted Phenanthroline Complexes: Intensities. *J. Chem. Soc. A* **1967**, 1536−1541.
(76) Peng, Q.; Niu, Y.; Shi, Q.; Gao, X.; Shuai, Z. Correlation Function Formalism for Triplet Excited State Decay: Combined Spin−Orbit and Nonadiabatic Couplings. *J. Chem. Theory Comput.* **2013**, *9*, 1132−1143.
(77) Scattergood, P. A.; Ranieri, A. M.; Charalambou, L.; Comia, A.; Ross, D. A. W.; Rice, C. R.; Hardman, S. J. O.; Heully, J.-L.; Dixon, I. M.; Massi, M.; et al. Unravelling the Mechanism of Excited-State Interligand Energy Transfer and the Engineering of Dual Emission in [Ir(C∧N)2(N∧N)]+ Complexes. *Inorg. Chem.* **2020**, *59*, 1785−1803.
(78) Baschieri, A.; Sambri, L.; Mazzanti, A.; Carlone, A.; Monti, F.; Armaroli, N. Iridium(III) Complexes with Fluorinated Phenyltetrazoles as Cyclometalating Ligands: Enhanced Excited-State Energy and Blue Emission. *Inorg. Chem.* **2020**, *59*, 16238−16250.
(79) Cazzaniga, M.; Cargnoni, F.; Penconi, M.; Bossi, A.; Ceresoli, D. Ab Initio Many-Body Perturbation Theory Calculations of the Electronic and Optical Properties of Cyclometalated Ir(III) Complexes. *J. Chem. Theory Comput.* **2020**, *16*, 1188−1199.
(80) Gao, Y.-J.; Zhang, T.-T.; Chen, W.-K. Predicting Excited-State and Luminescence Properties of a Cyclometalated Iridium(III) Complex: Quantum Mechanics/Molecular Mechanics Study. *J. Phys. Chem. C* **2021**, *125*, 5670−5677.
(81) Heil, A.; Marian, C. M. Structure−Emission Property Relationships in Cyclometalated Pt(II) β-Diketonate Complexes. *Inorg. Chem.* **2019**, *58*, 6123−6136.
(82) Monti, F.; Baschieri, A.; Sambri, L.; Armaroli, N. Excited-State Engineering in Heteroleptic Ionic Iridium(III) Complexes. *Acc. Chem. Res.* **2021**, *54*, 1492−1505.
(83) Motley, T. C.; Troian-Gautier, L.; Brennaman, M. K.; Meyer, G. J. Excited-State Decay Pathways of Tris(bidentate) Cyclometalated Ruthenium(II) Compounds. *Inorg. Chem.* **2017**, *56*, 13579−13592.
(84) Muro-Small, M. L.; Yarnell, J. E.; McCusker, C. E.; Castellano, F. N. Spectroscopy and Photophysics in Cyclometalated RuII−Bis(bipyridyl) Complexes. *Eur. J. Inorg. Chem.* **2012**, *2012*, 4004−4011.
(85) Oh-e, M.; Nagasawa, A. Advancing the a Posteriori Quest for Deep-Blue Phosphorescence: Quantifying Excitation-Induced Metal-to-Ligand Charge Transfer as a Guiding Indicator. *Organometallics* **2020**, *39*, 3951−3960.
(86) Bessho, T.; Yoneda, E.; Yum, J.-H.; Guglielmi, M.; Tavernelli, I.; Imai, H.; Rothlisberger, U.; Nazeeruddin, M. K.; Grätzel, M. New Paradigm in Molecular Engineering of Sensitizers for Solar Cell Applications. *J. Am. Chem. Soc.* **2009**, *131*, 5930−5934.

https://doi.org/10.1021/acsomega.2c07276
ACS Omega 2022, 7, 48583−48599

(87) Nguyen, T.-D.; Lin, C.-H.; Wu, C.-G. Effect of the CF_3 Substituents on the Charge-Transfer Kinetics of High-Efficiency Cyclometalated Ruthenium Sensitizers. *Inorg. Chem.* **2017**, *56*, 252−260.
(88) Shao, J.-Y.; Zhong, Y.-W. Stabilization of a Cyclometalated Ruthenium Sensitizer on Nanocrystalline TiO_2 by an Electrodeposited Covalent Layer. *Inorg. Chem.* **2019**, *58*, 3509−3517.
(89) Bomben, P. G.; Robson, K. C. D.; Sedach, P. A.; Berlinguette, C. P. On the Viability of Cyclometalated Ru(II) Complexes for Light-Harvesting Applications. *Inorg. Chem.* **2009**, *48*, 9631−9643.
(90) Feng, Z.; Wang, D.; Yang, X.; Jin, D.; Zhong, D.; Liu, B.; Zhou, G.; Ma, M.; Wu, Z. Asymmetric Heteroleptic Ir(III) Phosphorescent Complexes with Aromatic Selenide and Selenophene Groups: Synthesis and Photophysical, Electrochemical, and Electrophosphorescent Behaviors. *Inorg. Chem.* **2018**, *57*, 11027−11043.
(91) Wei, F.; Lai, S.-L.; Zhao, S.; Ng, M.; Chan, M.-Y.; Yam, V. W.-W.; Wong, K. M.-C. Ligand Mediated Luminescence Enhancement in Cyclometalated Rhodium(III) Complexes and Their Applications in Efficient Organic Light-Emitting Devices. *J. Am. Chem. Soc.* **2019**, *141*, 12863−12871.
(92) McCain, J.; Colón, K. L.; Barrett, P. C.; Monro, S. M. A.; Sainuddin, T.; Roque Iii, J.; Pinto, M.; Yin, H.; Cameron, C. G.; McFarland, S. A. Photophysical Properties and Photobiological Activities of Ruthenium(II) Complexes Bearing π-Expansive Cyclometalating Ligands with Thienyl Groups. *Inorg. Chem.* **2019**, *58*, 10778−10790.
(93) Weynand, J.; Moreno-Betancourt, A.; Loiseau, F.; Berthet, N.; Defrancq, E.; Elias, B. Redox-Active Bis-Cyclometalated Iridium(III) Complex as a DNA Photo-Cleaving Agent. *Inorg. Chem.* **2020**, *59*, 2426−2433.
(94) Bryant, G. M.; Fergusson, J. E.; Powell, H. K. J. Charge-Transfer and Intraligand Electronic Spectra of Bipyridyl Complexes of Iron, Ruthenium, and Osmium. I. Bivalent Complexes. *Aust. J. Chem.* **1971**, *24*, 257−273.
(95) Xie, P.; Chen, Y.-J.; Uddin, M. J.; Endicott, J. F. The Characterization of the High-Frequency Vibronic Contributions to the 77 K Emission Spectra of Ruthenium−Am(m)ine−Bipyridyl Complexes, Their Attenuation with Decreasing Energy Gaps, and the Implications of Strong Electronic Coupling for Inverted-Region Electron Transfer. *J. Phys. Chem. A* **2005**, *109*, 4671−4689.
(96) Chen, J.; Wang, J.; Deng, Y.; Li, B.; Li, C.; Lin, Y.; Yang, D.; Zhang, H.; Chen, L.; Wang, T. Novel cyclometalated Ru(II) complexes containing isoquinoline ligands: Synthesis, characterization, cellular uptake and in vitro cytotoxicity. *Eur. J. Med. Chem.* **2020**, *203*, No. 112562.
(97) Becke, A. D. Density-Functional Thermochemistry. III. The Role of Exact Exchange. *J. Chem. Phys.* **1993**, *98*, 5648−5652.
(98) Krishnan, R. B.; Binkley, J. S.; Seeger, R.; Pople, J. A. Self-Consistent Molecular Orbital Methods. XX. A Basis Set for Correlated Wave Functions. *J. Chem. Phys.* **1980**, *72*, 650.
(99) Perdew, J. P. Density-Functional Approximation for the Correlation Energy of the Inhomogeneous Electron Gas. *Phys. Rev. B* **1986**, *33*, 8822−8824.
(100) Perdew, J. P.; Burke, K.; Wang, Y. Generalized Gradient Approximation for the Exchange-Correlation Hole of a Many-Electron System. *Phys. Rev. B* **1996**, *54*, 16533−16539.
(101) Andrae, D.; Häußermann, U.; Dolg, M.; Stoll, H.; Preuß, H. Energy-Adjustedab Initio Pseudopotentials for the Second and Third Row Transition Elements. *Theor. Chim. Acta* **1990**, *77*, 123−141.
(102) Dunning, T. H.; Hay, P. J. Gaussian Basis Sets for Molecular Calculations. In *Modern Theoretical Chemistry*; Schaefer, H. F., Ed.; Plenum: New York, NY, 1977; pp. 1−28.
(103) Igel-mann, G.; Stoll, H.; Preuss, H. Pseudopotentials for Main Group Elements (Iiia through Viia). *Mol. Phys.* **1988**, *65*, 1321−1328.
(104) Tsai, C. N.; Tian, Y.-H.; Shi, X.; Lord, R. L.; Schlegel, H. B.; Chen, Y. J.; Endicott, J. F. Experimental and DFT Characterization of Metal-to-Ligand Charge-Transfer Excited States of (Rutheniumammine)(Monodentate Aromatic Ligand) Chromophores. *Inorg. Chem.* **2013**, *52*, 9774−9790.
(105) Tsai, C. N.; Mazumder, S.; Zhang, X. Z.; Schlegel, H. B.; Chen, Y. J.; Endicott, J. F. Metal-to-Ligand Charge-Transfer Emissions of Ruthenium(II) Pentaammine Complexes with Monodentate Aromatic Acceptor Ligands and Distortion Patterns of their Lowest Energy Triplet Excited States. *Inorg. Chem.* **2015**, *54*, 8495−8508.
(106) Tsai, C. N.; Mazumder, S.; Zhang, X. Z.; Schlegel, H. B.; Chen, Y. J.; Endicott, J. F. Are Very Small Emission Quantum Yields Characteristic of Pure Metal-to-Ligand Charge-Transfer Excited States of Ruthenium(II)-(Acceptor Ligand) Chromophores? *Inorg. Chem.* **2016**, *55*, 7341−7355.
(107) Lu, I. C.; Tsai, C. N.; Lin, Y.-T.; Hung, S.-Y.; Chao, V. P. S.; Yin, C.-W.; Luo, D.-W.; Chen, H.-Y.; Endicott, J. F.; Chen, Y. J. Near-IR Charge-Transfer Emission at 77 K and Density Functional Theory Modeling of Ruthenium(II)-Dipyrrinato Chromophores: High Phosphorescence Efficiency of the Emitting State Related to Spin-Orbit Coupling Mediation of Intensity from Numerous Low-Energy Singlet Excited States. *J Phys. Chem. A* **2021**, *125*, 903−919.
(108) Miertuš, S.; Scrocco, E.; Tomasi, J. Electrostatic Interaction of a Solute with a Continuum. A Direct Utilizaion of AB Initio Molecular Potentials for the Prevision of Solvent Effects. *Chem. Phys.* **1981**, *55*, 117−129.
(109) Scalmani, G.; Frisch, M. J.; Mennucci, B.; Tomasi, J.; Cammi, R.; Barone, V. Geometries and Properties of Excited States in the Gas Phase and in Solution: Theory and Application of a Time-Dependent Density Functional Theory Polarizable Continuum Model. *J. Chem. Phys.* **2006**, *124*, No. 094107.
(110) Tomasi, J.; Mennucci, B.; Cammi, R. Quantum Mechanical Continuum Solvation Models. *Chem. Rev.* **2005**, *105*, 2999−3094.
(111) Scalmani, G.; Frisch, M. J. Continuous Surface Charge Polarizable Continuum Models of Solvation. I. General Formalism. *J. Chem. Phys.* **2010**, *132*, 114110.
(112) Martin, R. L. Natural Transition Orbitals. *J. Chem. Phys.* **2003**, *118*, 4775−4777.
(113) Jakubikova, E.; Chen, W.; Dattelbaum, D. M.; Rein, F. N.; Rocha, R. C.; Martin, R. L.; Batista, E. R. Electronic Structure and Spectroscopy of [Ru(tpy)2]2+, [Ru(tpy)(bpy)(H2O)]2+, and [Ru(tpy)(bpy)(Cl)]+. *Inorg. Chem.* **2009**, *48*, 10720−10725.
(114) Frisch, M. J.; Trucks, G. W.; Schlegel, H. B.; Scuseria, G. E.; Robb, M. A.; Cheeseman, J. R.; Scalmani, G.; Barone, V.; Mennucci, B.; Petersson, G. A.; et al. *Gaussian 09, Revision A.02*; Gaussian, Inc.: Wallingford, CT, 2009.
(115) Seneviratne, D. S.; Uddin, M. J.; Swayambunathan, V.; Schlegel, H. B.; Endicott, J. F. Characteristics and Properties of Metal-to-Ligand Charge-Transfer Excited States in 2,3-Bis(2-pyridyl)-pyrazine and 2,2′-Bypyridine Ruthenium Complexes. Perturbation-Theory-Based Correlations of Optical Absorption and Emission Parameters with Electrochemistry and Thermal Kinetics and Related Ab Initio Calculations. *Inorg. Chem.* **2002**, *41*, 1502−1517.
(116) Hupp, J. T.; Williams, R. D. Using Resonance Raman Spectroscopy To Examine Vibrational Barriers to Electron Transfer and Electronic Delocalization. *Acc. Chem. Res.* **2001**, *34*, 808−817.
(117) Ertl, C. D.; Ris, D. P.; Meier, S. C.; Constable, E. C.; Housecroft, C. E.; Neuburger, M.; Zampese, J. A. Sticking and Patching: Tuning and Anchoring Cyclometallated Ruthenium(II) Complexes. *Dalton Trans.* **2015**, *44*, 1557−1570.
(118) Chen, Y.-J.; Xie, P.; Endicott, J. F.; Odongo, O. S. Probes of the Metal-to-Ligand Charge-Transfer Excited States in Ruthenium-Am(m)ine-Bipyridine Complexes: The Effects of NH/ND and CH/CD Isotopic Substitution on the 77 K Luminescence. *J. Phys. Chem. A* **2006**, *110*, 7970−7981.
(119) Chen, Y.-J.; Odongo, O. S.; McNamara, P. G.; Szacilowski, K. T.; Endicott, J. F. Metal-to-Metal Electron-Transfer Emission in Cyanide-Bridged Chromium−Ruthenium Complexes: Effects of Configurational Mixing Between Ligand Field and Charge Transfer Excited States. *Inorg. Chem.* **2008**, *47*, 10921−10934.
(120) Odongo, O. S.; Heeg, M. J.; Chen, Y.-J.; Xie, P.; Endicott, J. F. Effects of Excited State−Excited State Configurational Mixing on

https://doi.org/10.1021/acsomega.2c07276
ACS Omega 2022, 7, 48583−48599

Emission Bandshape Variations in Ruthenium−Bipyridine Complexes. *Inorg. Chem.* **2008**, *47*, 7493−7511.
(121) Chen, Y.-J.; Xie, P.; Heeg, M. J.; Endicott, J. F. Influence of the "Innocent" Ligands on the MLCT Excited-State Behavior of Mono(bipyridine)ruthenium(II) Complexes: A Comparison of X-ray Structures and 77 K Luminescence Properties. *Inorg. Chem.* **2006**, *45*, 6282−6297.
(122) Maruszewski, K.; Bajdor, K.; Strommen, D. P.; Kincaid, J. R. Position-Dependent Deuteration Effects on the Nonradiative Decay of the 3MLCT State of Tris(bipyridine)ruthenium (II). An Experimental Evaluation of Radiationless Transition Theory. *J. Phys. Chem.* **1995**, *99*, 6286−6293.
(123) Myers, A. B. Resonance Raman Intensities and Charge-Transfer Reorganization Energies. *Chem. Rev.* **1996**, *96*, 911−926.
(124) Fantacci, S.; Ronca, E.; De Angelis, F. Impact of Spin−Orbit Coupling on Photocurrent Generation in Ruthenium Dye-Sensitized Solar Cells. *J. Phys. Chem. Lett.* **2014**, *5*, 375−380.
(125) Ronca, E.; De Angelis, F.; Fantacci, S. Time-Dependent Density Functional Theory Modeling of Spin−Orbit Coupling in Ruthenium and Osmium Solar Cell Sensitizers. *J. Phys. Chem. C* **2014**, *118*, 17067−17078.
(126) Mori, K.; Goumans, T. P. M.; van Lenthe, E.; Wang, F. Predicting Phosphorescent Lifetimes and Zero-Field Splitting of Organometallic Complexes with Time-Dependent Density Functional Theory Including Spin−Orbit Coupling. *Phys. Chem. Chem. Phys.* **2014**, *16*, 14523−14530.
(127) Mishima, K.; Kinoshita, T.; Hayashi, M.; Jono, R.; Segawa, H.; Yamashita, K.; Lin, S. H. Theoretical Studies on the Absorption Spectra of cis-[Ru(4,4′-COO-2,2′-bpy)2(X)2]4−, (X = NCS, Cl) and Panchromatic trans-Terpyridyl Ru Complexes Including Strong Spin−Orbit Coupling. *Phys. Chem. Chem. Phys.* **2015**, *17*, 12317−12327.
(128) Yoshinaga, H.; Asada, T.; Koseki, S.; Yagi, S.; Matsushita, T. Spin−Orbit Coupling Analyses of Phosphorescence: the Effects of Cyclometalated Ligand Replacement in fac-Ir(ppy)3 with Various Bpy Ligands on Blue Phosphorescence. *RSC Adv.* **2016**, *6*, 65020−65030.
(129) Eskelinen, T.; Buss, S.; Petrovskii, S. K.; Grachova, E. V.; Krause, M.; Kletsch, L.; Klein, A.; Strassert, C. A.; Koshevoy, I. O.; Hirva, P. Photophysics and Excited State Dynamics of Cyclometalated [M(Phbpy)(CN)] (M = Ni, Pd, Pt) Complexes: A Theoretical and Experimental Study. *Inorg. Chem.* **2021**, *60*, 8777−8789.
(130) Mai, S.; Plasser, F.; Dorn, J.; Fumanal, M.; Daniel, C.; González, L. Quantitative Wave Function Analysis for Excited States of Transition Metal Complexes. *Coord. Chem. Rev.* **2018**, *361*, 74−97.

https://doi.org/10.1021/acsomega.2c07276
ACS Omega 2022, 7, 48583−48599